This manuscript was revised following one round of review at Journal of Petrology [Preprint; v. R1; 16th Feb 2026] , COPYRIGHTYEAR, pp. 1–57

DOI added during production

Advance Access Publication Date: Day Month Year

Paper

Biotite/melt trace-element, lithium, and F-OH partitioning in silicate magmas

Charles D. Beard,[1,2,3,*] Vincent J. van Hinsberg,[1] John Stix,[1]
Madeleine C.S. Humphreys,[4] Owen M. Weller,[2] Caroline R. Soderman[2]
and Jean H. Bédard[5]

[1]Dept. Earth & Planetary Sciences, McGill University, 3450 University St., Montreal, H3A 0E8, Québec, Canada
[2]Department of Earth Sciences, University of Cambridge, Downing Street, Cambridge, CB2 3EQ, UK
[3]Department of Earth Sciences, Utrecht University, Princetonlaan 8A, 3584 CB Utrecht, The Netherlands
[4]Department of Earth Sciences, Durham University, Science Labs, Stockton Road, Durham, DH1 3LE, UK
[5], Geological Survey of Canada, 491 de la Couronne, G1K 9A9, Québec, Canada

[*]Corresponding author. c.d.beard@uu.nl

Abstract

Biotite is a key hydrous silicate mineral in evolved magmatic systems, but its control on the behaviour of minor- and trace-elements, in particular Li, Nb, F and the REE is not well understood. Here, we quantify that control in sodic (per)alkaline H_2O-saturated magmas with variable F-content through crystallisation experiments at 650–800°C and 200 MPa total pressure, at log $fO_2 \approx$ FMQ +1. Biotite-glass pairs from tephriphonolite to phonolite fall deposits from Tenerife, Canary Islands, and a broad compilation from literature, complement our experimental data set. The new biotite-melt $Kd_{\mathsf{F/OH}}$ exchange coefficients are 2.9–47.0, typically 6.5–12.5, with minima for Al-rich, Mg-poor biotite. Nernst partition coefficients (D) for lithium are 0.24–32.8 with minima in F-poor biotite formed at high temperatures from peraluminous silicate melt. D values for the large alkali metal ions Na–Cs define Onuma parabolae consistent with their incorporation on the biotite $^{\mathsf{XII}}$A-site. Niobium partition coefficients are 0.1–1.2, and highest in Ti-rich biotite. The REE and actinides have D values less than 0.01 as their ionic radii fall between the size of the $^{\mathsf{XII}}$A-site and $^{\mathsf{VI}}$M-sites of biotite. Our data, alongside a literature compilation, constrain empirical models that: (1) describe the exchange of F and OH between the silicate melt and the biotite W-site; (2) predict the partitioning of 1+ cations Li–Cs between silicate melt and the biotite A- and M-sites; (3) predict D_{Nb} values. The models use the major-element composition of biotite and silicate melt, pressure and temperature as input. Models are calibrated for use over a wide range of pressure, temperature and bulk composition (P-T-X) and can be used to interrogate biotite from natural systems to determine the composition of their source melt, or to forward model the trace-element evolution of mafic to evolved peralkaline syenite or peraluminous granite systems at upper-mantle to crustal pressures.

Keywords Experimental petrology; Halogens; Mica group; Partition coefficient; Pegmatite

---

Received: Date Month Year. **Revised received:** Date Month Year. **Accepted:** Date Month Year

© The Author(s) COPYRIGHTYEAR. Copyright and licence statements to be updated by the publisher during production.

Introduction

Biotite forms in a wide variety of natural settings and is estimated to comprise up to 8% of the exposed continental crust (Nesbitt & Young, 1984). The biotite series are trioctahedral micas with a structure that comprises two opposing sheets of tetrahedrally-coordinated cations, with a sheet of larger octahedrally-coordinated cations sandwiched between (Rayner 1974; Brigatti & Guggenheim 2002; Fleet 2003; see inset to Fig. 7 below). Biotite mica has the general formula $\mathrm{A\,M_3\,T_4\,O_{10}\,W_2}$ where A are large, dominantly monovalent, interlayer cations that are twelve-fold coordinated (K, Na, Ba), M are octahedrally coordinated cations (Li, Mg, Fe^{2+}, Al, Fe^{3+}, Ti) split into two M1 sites and one slightly smaller M2 site, T are tetrahedrally coordinated cations (Si, Al, Fe^{3+}), and W (sometimes known as the X- or OH-site) are dominantly monovalent anions that are positioned perpendicular to the plane of the silicate sheets (OH^-, F^-, O^{2-} with minor Cl^-).

The composition of igneous biotite tracks that of their co-existing melts, with Mg-rich phlogopite stable in calc-alkaline arc systems and in small-fraction lithospheric mantle melts (e.g., Abdel-Rahman, 1994; LaTourrette *et al.*, 1995; Ezad & Foley, 2022), and Fe^{2+}-rich annite stable in (per)alkaline magmatic systems (Finch *et al.*, 1995; Möller & Williams-Jones, 2016). Trioctahedral micas in peraluminous granites are mostly magnesian annite ($Fe^{2+}/(Fe^{2+}+Mg)$ = 0.63–0.68), with high M-site Al contents (^{M}Al = 0.35–0.64 cpfu; Brigatti & Guggenheim 2002) whereas biotite in metaluminous, commonly I-type granites such as the Sierra Nevada batholith in California, USA have intermediate $Fe^{2+}/(Fe^{2+} + Mg)$ of ca. 0.48–0.41, and low Ti content up to 0.02 cpfu (Gray *et al.*, 2008).

As a major hydrous silicate mineral in both crustal and upper mantle environments, biotite is an important host for volatile components including water, fluorine (London, 1997; Grégoire *et al.*, 2002; Dolejš & Baker, 2007; Aiuppa *et al.*, 2009; Ezad & Foley, 2022) and lithium (Ellis *et al.*, 2022; Kunz *et al.*, 2022; Neukampf *et al.*, 2023). Most igneous biotite have molar $F/(F + Cl + OH) < 0.4$, with biotite hosting 70–90% of the F in muscovite- and fluorite-free granitoids (Speer, 1984). Mg-F rich metasomatic biotite has been reported from Mt Etna and a number of other potassic volcanoes in Italy (Gianfagna *et al.*, 2007) and is associated with porphyry copper deposits (Speer, 1984).

The behaviour of the halogen fluorine is of particular interest because it reduces both the liquidus and solidus temperature of most silicate assemblages (Wyllie & Tuttle, 1961), the viscosity of silicate melts (Dingwell *et al.*, 1985) and impacts the mineralogy and major-element composition of crystallising phases (Giehl *et al.*, 2014; Beard *et al.*, 2020). In alkaline-silicate systems, fluorine is thought to play a key role in the orthomagmatic enrichment of the REE, HFSE and U (London, 1987; Linnen *et al.*, 2012; Marks & Markl, 2017; Siegel *et al.*, 2018; Beard *et al.*, 2023). This role is, at least in part, because fluorine complexes directly with REE in silicate melt (Ponader & Brown Jr., 1989) and influences the medium-range structural environment around HFSE^{4+} cations (Farges, 1996), reducing their activity and thus availability for incorporation into silicate minerals (Beard *et al.*, 2020). The limited effect of fluorine on the solubility of Mn-columbite and Mn-tantalite, and small positive effect on the solubility of zircon and hafnon indicates that fluorine has a smaller influence on the budget of 5+ and 4+ HFSE cations in magmas relative to REE (Aseri *et al.*, 2015). Temperature and melt ASI (molar $Al_2O_3/(Na_2O + K_2O + CaO)$ appear to be the dominant controls on HFSE phase saturation. Fluorine in the melt thereby promotes residual enrichment of the REE and, to a lesser extent, HFSE during crystallisation of alkaline magmatic systems. To a certain degree fluorine, along with the alkalies, explains the high concentration of REE and HFSE in some of the most evolved peralkaline rocks. Fluorine can also trigger liquid immiscibility, which can further segregate and concentrate the REE and HFSE (Vasyukova & Williams-Jones, 2016; Yang & van Hinsberg, 2019).

Because biotite has the highest Li concentration of the major mineral phases in alkaline and calc-alkaline volcanic suites, the crystallisation or destabilisation of biotite represents a major control on the lithium budget of silicate melts, and of crustal igneous systems globally (Ellis *et al.*, 2022; Neukampf *et al.*, 2023). Major economic deposits of lithium occur in LCT (Li-Cs-Ta) pegmatites associated with evolved peraluminous igneous systems (Linnen *et al.*, 2012; London, 2018; Gardiner *et al.*, 2024). However, forward modelling of the processes responsible for the enrichment of their contained lithium have mostly been limited to use of fixed $D_{\mathrm{Li}}^{mineral/melt}$ values (e.g., Koopmans *et al.* 2024), despite broad reported variation that spans incompatible to compatible behaviour (see Horányi *et al.* 2025; Morris *et al.* 2026, accepted). Only a few studies have presented experimental Li partition coefficients (Icenhower & London, 1995; LaTourrette *et al.*, 1995; Schmidt *et al.*, 1999; Evensen & London, 2002; Adam & Green, 2006; Pichavant *et al.*, 2016; Horányi *et al.*, 2025) most likely due to challenges with analyses of Li via EPMA, and contamination of ICP-MS instruments with lithium metaborate flux.

None to our knowledge have presented continuous functions that describe lithium partitioning among biotite and silicate melt.

Biotite has been produced experimentally over a wide range of temperatures and pressures (500–1430 °C, 1 atm to 5 GPa, LEPR database; Hirschmann *et al.*, 2008), with Mg-rich biotite stable at high temperature and pressure relative to Fe-rich varieties. The presence of fluorine expands biotite stability to higher temperatures (by up to ∼500 °C; Munoz 1984; Peterson *et al.* 1991) and to atmospheric pressure (e.g. Hammouda & Cherniak, 2000).

Experimental investigations have also studied biotite-melt partitioning of minor- and trace-elements at a range of conditions, including in mafic bulk compositions at upper mantle pressures (15–30 kbar; Guo & Green 1990; LaTourrette *et al.* 1995; Schmidt *et al.* 1999; Green *et al.* 2000; Adam & Green 2006), granitic systems (Icenhower & London, 1995, 1997; Lukkari & Holtz, 2007) and moderately evolved alkaline silicate compositions at upper crustal pressures (0.76–2 kbar; Righter & Carmichael 1996; Fabbrizio & Carroll 2008; Zhang *et al.* 2022). These element partitioning studies indicate that biotite readily incorporates the LILE and HFSE, but not the REE or actinides (see compilation in Appendix B). However, none of these studies targeted peralkaline systems, where F-OH exchange may be influenced by short-range order between F and excess alkalies in the silicate melt (Dolejš & Baker, 2006) and trace-element partitioning may be controlled by different exchange mechanisms relative to those active in less-evolved igneous systems (cf. Beard *et al.* 2019).

Here, we investigate the effects of biotite composition and temperature on the uptake of minor- and trace-elements in silica-undersaturated alkaline and peralkaline silicate melts at varying F contents. We combine experiments at 200 MPa with biotite phenocryst-glass pairs from phonolitic pumice fall deposits, and collate biotite-melt partitioning experiments from the literature that simulate mafic to evolved systems, including granites. We then characterise the mineral and melt compositional controls on element partitioning behaviour and present empirical models for fluoride-hydroxyl exchange (cf. Riker *et al.* 2018; Zhang *et al.* 2022), the partitioning of Li and Nb, and a lattice-strain model for partitioning of the large 1+ ions Na–Cs. These new element partitioning models can be used to predict the evolution of element budgets during magmatic differentiation, as well as providing a tool to reconstruct parental melt compositions from analyses of biotite in natural igneous rocks.

Methodology

Experimental techniques

Biotite was synthesised in sodic alkaline melts of tephriphonolite to phonolite composition to obtain a range of mineral compositions consistent with those in natural alkaline-silicate magmas. Three synthetic, trace-element doped starting glass compositions were investigated (compositions M3, M5 and H5 from Beard *et al.*, 2019, Table 1), and fluorine was added to some of the charges as trace metal grade 40% hydrofluoric acid (Beard *et al.* 2020; see Appendix B). Powders of starting glass (0.125–0.190 g) were loaded into platinum capsules of 3.0–3.5 mm internal diameter and 16–25 mm length, with distilled water in excess of saturation ± HF added immediately prior to closure and welding. Capsule mass was monitored throughout the loading procedure and verified after the experiments to check for leaks.

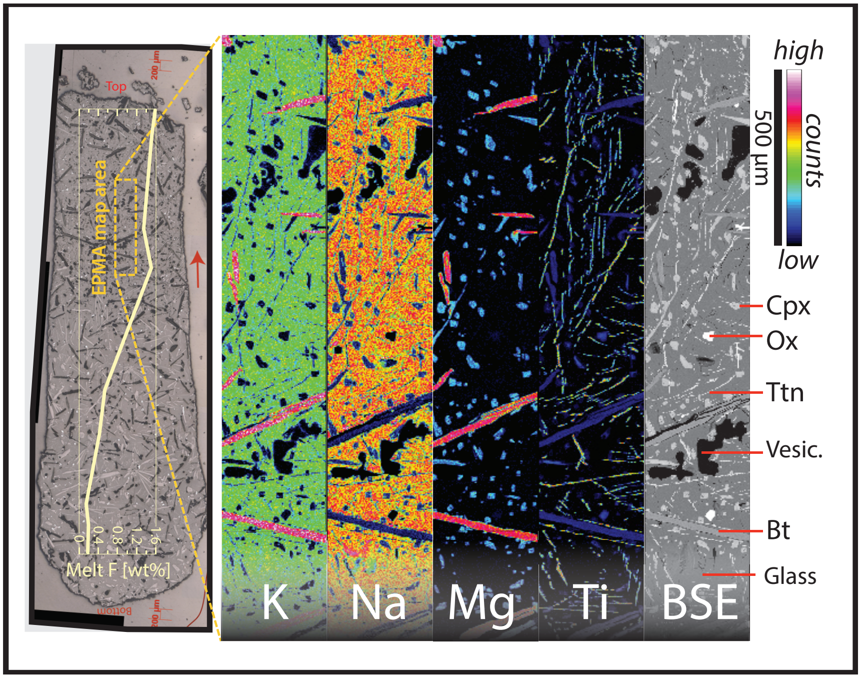

Figure 1 Reflected light micrograph and major-element abundance maps for experiment M3 1.25F, as measured by wavelength dispersive spectrometry. The thick cream line in the left panel shows the melt fluorine content at each vertical interval averaged over the capsule width. Bt = biotite; Cpx = clinopyroxene; Ttn = titanite; Ox = Fe oxide minerals; Vesic. = vesicle of aqueous fluid.

Crystallisation experiments were conducted in Pt capsules in a Harwood-type internally heated pressure vessel in the HP-GeoMatS laboratory at the GeoForschungsZentrum, Potsdam, Germany. Run temperatures were chosen between liquidus and solidus for each of the compositions of interest, corresponding to 650 to 800°C at 200 MPa total pressure. Oxygen fugacity was buffered using an Ar-H_2 gas pressure medium, with exchange of H_2 through the experiment capsule walls resulting in log $fO_2 \approx \Delta\text{FMQ} +1$ in our H_2O-saturated charges (see Berndt *et al.* 2002; Jugo *et al.* 2010). Our vessel did not feature a Shaw membrane for measurement and control of H_2 fugacity (Berndt *et al.*, 2002). Charges were placed into the apparatus, pressurised, then homogenised at 1100–1200°C for at least 16 h. Following homogenisation, the charges were cooled to run temperature at 1°C/min to facilitate slow growth of crystals and to impede development of melt heterogeneities adjacent to phase boundaries. Temperature was then cycled twice between run temperature and run temperature + 10°C to encourage dissolution of small crystals at the expense of larger grains, and to promote crystal growth close to the run temperature (one cycle equals 30 min at T_{run}, 30 min at T_{run} + 10°C, then cooling to T_{run} at 1°C/min). The final run temperature was held for >45 h to allow for homogenisation of the melt and Ostwald ripening of the biotite crystals. Capsules were then quenched to room temperature. Wherever possible, rapid quench apparatus was used to limit the growth of groundmass crystals. Here, the vessel was mounted vertically on a trunion, with capsules hung from a fusible Pt wire allowing them to fall out of the hot zone on experiment termination. Even without rapid quench apparatus, cooling to below the glass transition ($<$ 350°C; Giordano *et al.* 2005) was achieved in less than 150 seconds. Following quench the capsules were weighed, pierced, dried and re-weighed, which confirmed in all cases the presence of a free fluid phase. Capsules were then torn open with pliers and charges split along their vertical axis with a low-speed wafering saw. Half of each charge was mounted in epoxy and polished for microanalysis (Fig. 1). A more detailed experimental methodology is presented in Beard *et al.* (2019, 2020).

Natural samples

Biotite crystals were separated from fifteen pyroclastic deposits from the Canary Islands with basanitic to phonolitic compositions (Appendix A, see Beard *et al.* 2019). The pumices and scoria were rinsed under tap water, dried at 110°C overnight, then gently hand crushed with a hammer. Crystals and glass fragments were hand-picked from sieved size fractions of 125–1180 µm, and 5–20 crystals of biotite from each sample were mounted in epoxy for microanalysis. The pyroclastic rocks also contain augite clinopyroxene, anorthoclase to sanidine feldspars, ± spinel, ± amphibole, ± olivine, ± titanite, ± sodalite (see analyses in Beard *et al.*, 2019). The glass analysed for partition coefficients was adhered to the walls of the mounted clinopyroxene crystals.

The Canaries biotite are elongate faceted crystals with vesicular glass adhered to the surface of some grains (Fig. 2). The mounted biotite crystals were examined using backscattered electron imagery and all from the selected samples appeared to be free of chemical zoning.

Biotite crystals from all of the samples were analysed by electron probe microanalyser (EPMA) to determine their major-element composition (Fig. 3). A subset of four samples were selected for determination of apparent biotite/melt trace-element partition coefficients by laser ablation ICP-MS (Appendix B). These samples were chosen because, in addition to biotite, they contain unzoned crystals of clinopyroxene, a mineral that readily records chemical and physical perturbations to the magmatic system during growth (e.g., Ubide *et al.* 2019; Masotta *et al.* 2020). The clinopyroxene-melt pairs within these fall deposits preserve near-equilibrium crystallisation (Beard *et al.*, 2019), and their biotite most probably formed under similar conditions. The samples comprise phonolitic, plinian fall deposits from the $\sim$ 2 ka eruptions of Montaña Blanca (units LMB and UMB-II) and Pico Viejo, Tenerife (Ablay *et al.*, 1995), as well as a basanite pyroclastic deposit from Montaña Samara, a monogenetic cinder cone, also on Tenerife (Albert *et al.*, 2015). Pre-eruptive magma storage conditions for Montaña Blanca unit UMB-II have been constrained with phase equilibrium experiments to be 850±15°C, 50±20 MPa, with 2.5±0.5 wt% H_2O at log $fO_2 \approx \Delta$NNO –0.5 (Andújar & Scaillet, 2012).

Analytical techniques

Electron probe analysis

Major-element compositions of the experiment run products and natural biotite and glass were measured using a JEOL 8900 instrument at McGill University and a JEOL 8230 instrument at the University of Ottawa, with analyses calibrated using natural mineral standards. Biotite crystals were measured with a 15 nA beam of 2–5 µm diameter, accelerated by a potential of 15 kV. Quenched melts were measured with a 4 nA beam of 50 µm diameter. At Ottawa, all major-elements, including fluorine, were measured for 60 s. At McGill, counting times for the elements Al, K, Fe, Na, Si, Mg and Ca were 20 s, Cl 30 s, Ti 40 s and F 150 s. For fluorine, a notoriously challenging element to measure, we used TAP diffraction crystals with intensities calibrated against natural fluorite reference materials. Fluorine detection limits at Ottawa were ∼ 275 ppm and at McGill were ∼ 1100–3600 ppm. With these routines, we observed no sodium loss, nor amplification of signals for the rest of the major-elements over the measurement time period (e.g., Al, F; Morgan vi & London 2005). Melt compositions for the Canary Islands rocks were determined by analyses of glass rims adhered to clinopyroxene grains separated from the same samples (see Beard *et al.*, 2019).

Data for two mica and twelve glass secondary standards are in Appendix B. Reproducibility of major and minor element oxide abundance in mica standards is 1–7% RSD (1σ) and for F and Cl is 8.7–13.6%. Accuracy relative to GeoRem compiled values is better than 10%, except for Na and Cl, which are within 20%. Glass secondary standard reproducibility ranges from 0.17–1.06% for SiO_2 and is better than 5% for most major elements (¿1 wt.%).

Laser ablation ICP-MS

The trace-element concentrations of biotite crystals and glass were measured with a NewWave 213 nm Nd-YAG laser system coupled to a Thermo Finnigan iCAP-Qc quadrupole ICP-MS instrument at McGill University. A pulse frequency of 10 Hz was used, and beam fluence was typically 6–10 J/cm^2. Ablated material was carried to the ICP-MS instrument in a He flow of 800 mL/min and mixed with Ar prior to injection into the plasma. The primary standard glass BCR-2G was used to monitor and correct for drift, and accuracy was determined by the analyses of secondary standards NIST-610, USGS-RGM-1 rhyolite, UTR-2 peralkaline rhyolite glass, and Mg-mica and Fe-mica reference materials. Sample surfaces were pre-ablated to remove residues from polishing and to improve coupling between the laser beam and sample. A list of analytes with typical precision, as determined from multiple analyses of reference materials, is given in Appendix B.

Experiment biotite crystals were measured with a beam of 12–40 µm diameter, along line scans of 4–12 µm/s, with 5–15 grains measured per experimental charge. To minimise downhole fractionation among analytes we used faster scans where target phases required a smaller beam size. Experiment glass was measured with a beam size of 20–60 µm along line scans at 4–8 µm/s, and 8–16 areas of glass were measured per charge. These settings resulted in ca. 4–60 sec of signal per analysis. Canary Islands biotite crystals were analysed along line transects at 4 µm/s with a beam of 40 µm diameter and fluence

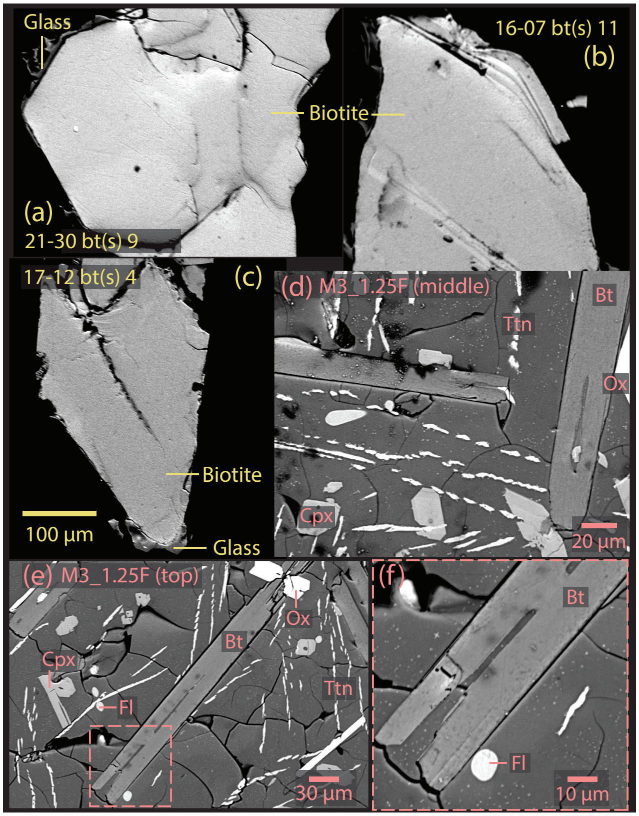

Figure 2 Canary Islands biotite (a–c; yellow annotations, all same scale) are faceted and show no zonation in backscattered electron images (BSE). Some have vesicular glass adhered to their margins. Experiment biotite (d–f; pink annotations) also show no zonation in BSE, and commonly preserve melt inclusions. Occasionally, biotite also enclose clinopyroxene (d). Bt = biotite; Cpx = clinopyroxene; Ttn = titanite; Ox = Fe oxide mineral; Fl = fluorite.

of 9.5 J/cm^2. A total of 4–10 crystals of biotite were measured per sample. Corresponding quenched melts were measured with a static beam of 20–30 µm.

Drift corrections and data reduction were performed with the Iolite v2.5 software (Paton *et al.*, 2011), running in the Igor Pro environment. For the glass and Canary Islands biotite, the Al concentration from electron probe analyses was used as an internal standard. For the majority of biotite crystals in the experimental charges, mixed analyses of biotite and glass resulted. In this case, a robust linear unmixing model was applied to determine the trace-element composition of these crystals using their Mg/Al ratio as determined by electron probe to constrain mixing ratios (see Appendix C, cf. Rubatto & Hermann 2007; Yang *et al.* 2018; Beard *et al.* 2019, 2020). For some samples, glass analyses by LA-ICP-MS also required unmixing, and here the mixing ratio was constrained using the Na/Al ratio as determined by

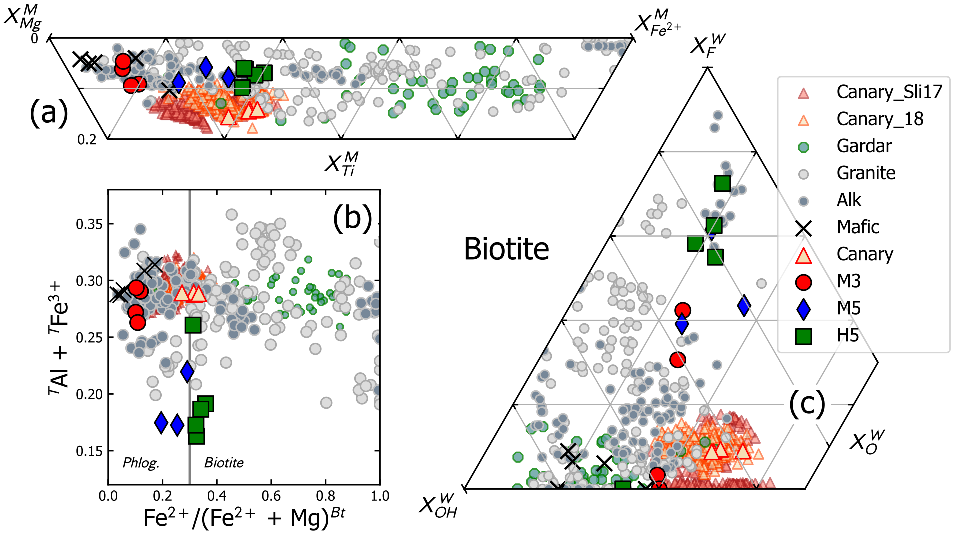

Figure 3 Major-element compositions of biotite from the Canary Islands pyroclastic rocks, compared with those produced in the experiments. (a) M-site Fe^{2+}, Mg, Ti ternary diagram; (b) Tetrahedral Al + Fe^{3+} vs. $Fe^{2+}/(Fe^{2+}+Mg)$ ratio for biotite; (c) W-site F^-, OH^-, O^{2-} ternary diagram. Lattice site occupancies are calculated based on a total cation charge of 22 per formula unit following Li *et al.* (2020). Literature experiment biotite are divided into: Granite, Alk, and Mafic based on their glass compositions (Full references in Appendix B). Canary Islands biotite compilations not used in determination of partition coefficients from Sliwinski *et al.* (2017) and Beard (2018). Gardar Province biotite from Finch *et al.* (1995).

electron probe analysis. A series of three MATLAB scripts for reduction of laser ablation data from both unmixed and mixed analyses are available in Appendix C.

Results

Experiment run products

Results were obtained for eight experimental charges (Tables 2–3). The experiments equilibrated at near-liquidus conditions (< 35% crystals, Figs. 1, 2), and glass in most charges is free of quench crystals. Charges run without fluorine are homogeneous with respect to melt composition and phase proportions, containing an assemblage of quenched melt, aqueous fluid, biotite, sodic clinopyroxene ± magnetite ± titanite ± alkali feldspar. Charges run with fluorine contain quenched melt, aqueous fluid, biotite ± sodic clinopyroxene ± Fe-oxide ± F-rich titanite ± fluorite ± a F-Ti-Ca-Na phase with a composition consistent with the sorosilicate minerals hiortdahlite and kochite. The fluorine-bearing

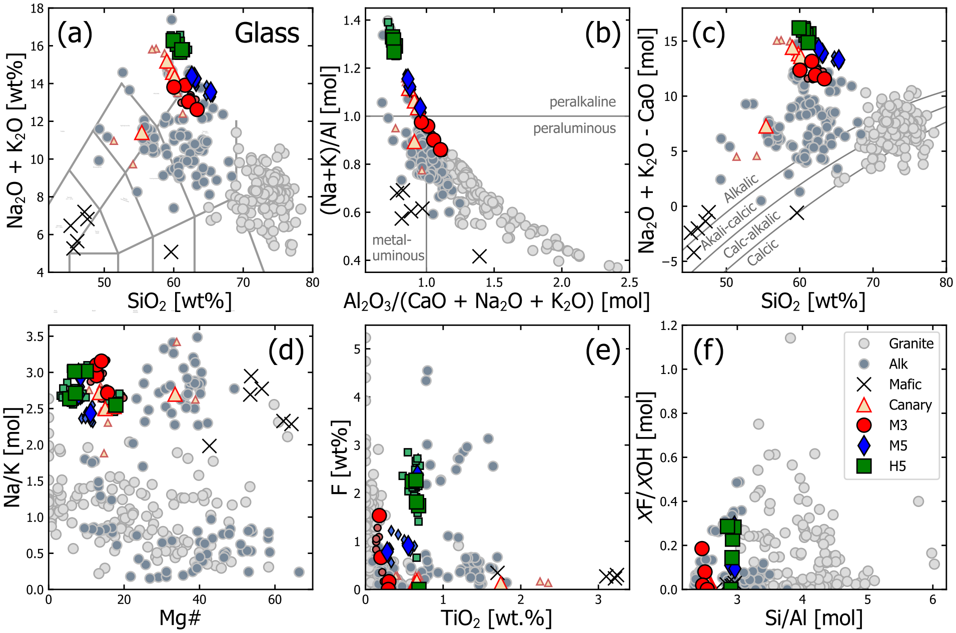

Figure 4 Major-element compositions of quenched melt from experiments and Canary Islands pyroclastic rocks (subset for partitioning). Small symbols are individual EPMA points, and larger ones are averages per experiment zone or natural sample. Literature data for 'Alk', 'Mafic', and 'Granite' as in Figure 3. (a) is a total alkalies vs. silica diagram, showing that our experiment quenched melts are trachyte to phonolite in composition; (b) shows their per-/metaluminous to peralkaline compositions; (c) shows glass compositions on a granite classification diagram from Frost *et al.* (2001); (d) shows their low Mg# and high Na/K compositions; (e) shows glass TiO_2 and F content, and; (f) the proportion of F^- to OH^- anions versus molar Si/Al ratio.

charges are internally zoned, with higher quenched melt fluorine contents and greater modes of fluorine-rich biotite and titanite toward their top, grading to clinopyroxene-rich assemblages toward their bottom (maximum melt F variation in a single capsule was 0.16–1.57 wt.%; see Fig. 1). Vertical variation in fluorine concentration results from addition of concentrated HF to the top of capsules and subsequent downward migration of fluorine through the charges. The concentration of other major-elements in quenched melt show limited variation with position in the capsule, with small offsets associated with changes to phase relations that follow melt fluorine. While capsule-wide equilibrium was not attained, our earlier Cpx/melt study that uses these same charges demonstrated close approach to local equilibrium between minerals and melt (Beard *et al.*, 2020). Phase relations and Cpx/melt partition coefficients are similar among charges with differing fluorine concentration gradients, as well as with unzoned charges where fluorine was pre-homogenised throughout the starting glass. A detailed description of the textures, phase relations and variations in melt chemistry, and a discussion of the implications of capsule stratification are presented in Beard *et al.* (2020).

Capsules with a melt fluorine gradient are split into up to five zones for a total of 39 zones including the fluorine-free compositions. A total of twelve zones contain biotite and are discussed below.

Biotite compositions

Major-element compositions of the experiment and natural biotite are given in Table 2 and Figure 3 & S1. Major- and minor-element ions were assigned to lattice sites following the method of Li *et al.* (2020), including the Fe^{2+}/Fe^{3+} ratio, Li, and the proportions of fluorine, hydroxyl, O^{2-} and chlorine at the biotite W-site (calculations are for a charge of 22 per formula unit). This method is based on a principle component regression machine learning model, calibrated on a training set of 155 biotite references with measured chemistry and crystal structural refinement. Absolute errors reported for this model are ± 0.2 apfu for octahedral Fe^{2+}, octahedral Al^{3+} and OH^- at the W site, and ± 0.3 apfu for total Fe^{3+} and $^{W}O^{2-}$.

Biotite crystals from the experiments are phlogopite to fluorophlogopite following Rieder *et al.* (1998), with molar Mg# of 57–78, tetrahedral Al of 0.43–1.14 c.f.u., octahedral Al of 0.04–0.34 c.f.u, Ti of 0.13–0.26 c.f.u. and F contents of 0–1.45 a.f.u (Fig. 3). With increasing fluorine content in the synthesised biotite, ^{IV}Al exchanges for ^{IV}Si (Fig. S1a), and ^{VI}Ti exchanges for ^{VI}Mg (Fig. S1b), the latter consistent with the Ti-oxy-hydroxide coupled substitution mechanism reported by Schmidt *et al.* (1999):

$$\begin{gathered}[^{M}\mathrm{Mg}^{2+} + 2\,^{W}(\mathrm{OH}^-,\ \mathrm{F}^-)]_{\mathrm{Bt}} + \mathrm{Ti}^{4+}_{\mathrm{melt}} + 2\,\mathrm{O}^{2-}_{\mathrm{melt}} \rightleftharpoons \\ [^{M}\mathrm{Ti}^{4+} + 2\,^{W}\mathrm{O}^{2-}]_{\mathrm{Bt}} + \mathrm{Mg}^{2+}_{\mathrm{melt}} + 2\,(\mathrm{OH}^-,\ \mathrm{F}^-)_{\mathrm{melt}}\end{gathered} \tag{1}$$

Further, potassium at the A-site increases at the expense of sodium with increasing fluorine at the biotite W site. These trends are observed across all experiment bulk compositions.

The Canary Islands crystals selected for this partitioning study (large triangles in Fig. 3) are phlogopite to biotite in composition and sit toward the upper end of the X^{M}_{Ti} and Fe^{2+}/Fe^{2+} + Mg) range defined by a larger Canaries biotite dataset (including our measurements and those from Sliwinski *et al.* 2017). They show no notable zonation in BSE intensity across grains, suggesting minimal compositional variation during growth (Fig. 2). When compared to our experiment biotite, the Canaries minerals extend the compositional range to slightly lower Mg# (54–72), higher $^{\mathrm{IV}}$Al (1.05–1.30 c.f.u.) and Ti (0.23–0.44 c.f.u.), and have a narrower range of F contents (0.05–0.30 a.f.u). The Canary Islands biotite follow compositional trends defined by the experiment biotite and additionally display a positive correlation between Mn and F content (the experiments are Mn-free).

The most abundant trace-elements in both the experiment and natural biotite are Ba and Rb (ca. 100–3700 & 200-350 µg/g, respectively). Our Canary Islands biotite have Ba, Zr, Sr and Nb concentrations that fall within the typical range for biotite from Tenerife zoned phonolitic ignimbrites (Sliwinski *et al.*, 2017). They have Li contents of 3.5–28 µg/g and REE contents close to or below the detection limit of our setup (ca. 0.1 µg/g).

Glass compositions

Quenched silicate melts from the experiments are trachyte and phonolite on the TAS classification of Le Maitre *et al.* (2005), with molar (Na + K)/Al of 0.86–1.34, Mg# of 6–14, and F contents of up to 2.85 wt.% (Fig. 4). The final experiment glasses have higher SiO_2 and lower FeO_T, MgO and CaO relative to their respective starting material, consistent with crystallisation of the produced mineral phases. A superliquidus experiment using the H5 composition lost 0.82% FeO_T relative to its starting glass via alloying with the Pt capsule (see Beard *et al.* 2019). This alloying phenomenon will contribute to changes in experiment Mg#, but is not enough to explain the all of the Fe-Mg systematics of the experiment glass data set. The Canary Islands tephra glasses are tephriphonolite and phonolite and overlap with the composition of experiment glass with molar (Na + K)/Al 0.78–1.16 and F contents <0.07–0.28 wt.%. Canary Islands glass extends to higher Mg# (13–39) than the experiments.

All experiments produced an aqueous fluid phase in addition to silicate melt. The water content of the silicate melt was estimated as 6.19–7.62 wt.% using a solubility model calibrated on andesite and rhyolite compositions that takes into account the effects of fluorine (Zhang *et al.*, 2022). The model assigns water dissolved in the silicate melt to molecular water (H_2O_m) and hydroxyl species (OH^-) using equilibrium constants for water dissociation from Botcharnikov *et al.* (2006), which are optimised for andesitic melts. This approach is valid as there is little variation in water dissociation constants between rhyolitic and basaltic melts (Behrens, 2020). Following this scheme, $X_{\mathrm{F}}/X_{\mathrm{OH}}$ for the quenched melt in our fluorine-bearing experiments is 0.02–0.29. The melt ratio of non-bridging oxygen anions per tetrahedrally coordinated cation (NBO/T) was calculated following Mills (1993). This calculation method does not consider the potential role of ferric iron, nor that of water or the halogens. It was chosen to maximise applicability of our empirical models, especially considering scenarios where only routine whole-rock geochemical measurements have been made.

Discussion

The attainment of equilibrium between biotite and silicate melt

Close approach to local equilibrium in the experiments is indicated by consistency of results among duplicate charges, and in the case of experiments with vertical zonation in fluorine content, in vertical zones within charges (see below, for both Cpx/melt and Bt/melt D values; cf. Beard *et al.* 2020) and the presence of mineral phases with limited to no chemical zoning. Biotite crystals from our experiments are homogeneous with respect to major-element compositions, as determined from EPMA mapping (Fig. 1), although they are too small to assess whether zonation of trace-elements is present. Quenched melts are homogeneous with respect to both major- and trace-elements, showing no discernible gradients in composition adjacent to crystal boundaries. Zonation of lanthanides within clinopyroxene from the same experiments is minimal (Beard *et al.*, 2019, 2020), suggesting that trace-element zonation within the experimental biotite would also be minor.

Numerous fluorine-bearing charges in this study are vertically-zoned (Fig. 1), an effect attributed to the incomplete homogenisation of fluorine, which was added as concentrated HF to the top of the capsules (see discussion in Beard *et al.* 2020). For these charges, local equilibrium between the minerals and melt is demonstrated by the following observations: (1) minerals and glass have the same composition within horizontal bands of equal melt F content among separate experimental charges; (2) charges with pre-homogenised fluorine contents (added as NaF & KF powders) developed similar mineral and melt compositions for a given melt fluorine content, and return similar mineral/melt D values (Beard *et al.*, 2020); and (3) mineral compositions, melt compositions and partitioning behaviour are consistent among experiments and natural samples, including literature data (Figs 3,4 and below).

Homogenisation of major and trace-element concentrations within the mica structure is generally assumed to occur quickly relative to that of inosilicates and the feldspar minerals, because biotite in natural igneous systems rarely displays zonation (e.g., optical zonation related to composition, Deer *et al.*, 1992). Biotite grains that preserve major-element or trace-element zoning have been reported for volcanic systems and pegmatites (Sliwinski *et al.*, 2017; Azadbakht & Lentz, 2020). The experimental diffusion database for micas is limited, with published studies focused on the diffusion of LILE cations, Ar, O, H, and the OH-F exchange (see review by Cherniak & Dimanov, 2010). For Sr, the activation energy for diffusion in mica is significantly lower than that for hornblende, which in turn is lower than for diopside. Diffusion in melt is faster. It can thus be assumed that our experiment biotite and glass compositions represent the equilibrium partitioning of elements at the run conditions.

In the Canary Islands samples, biotite is unzoned in backscattered electron images (e.g., Fig. 2), and the compositional consistency between crystals in each pyroclastic fall sample supports the hypothesis of equilibrium. This interpretation is further corroborated by the presence of unzoned clinopyroxene in the same samples that record a relatively constant physical and chemical environment in the magma chamber during crystal growth (see Beard *et al.*, 2019). Icenhower & London (1997) suggested that fluorine partition coefficients determined from pyroclastic rocks are biased toward higher values due to oxidation reactions and reequilibration associated with degassing and decline of the $f\mathrm{H_2O}/f\mathrm{HF}$ ratio of biotite. We do not see F-rich rims on biotite from our Canary Islands rocks, suggesting this phenomenon does not affect our results.

F-OH exchange between biotite and silicate melt, and implications for Ti-in-biotite thermometry

Biotite incorporates fluoride as a structural anion, replacing as much as 100% of the $\mathrm{OH^-}$ and $\mathrm{O^{2-}}$ anions (e.g., Fig 3c), and can therefore exert a major control of the fluorine budget of alkaline-silicate magmatic systems (Speer, 1984; Munoz, 1984). Fluoride can be incorporated into biotite via the following exchange reaction:

$$^{\mathrm{W}}\mathrm{OH}^-_{\mathrm{Bt}} + \mathrm{F}^-_{\mathrm{melt}} \rightleftharpoons \mathrm{OH}^-_{\mathrm{melt}} + {}^{\mathrm{W}}\mathrm{F}^-_{\mathrm{Bt}} \qquad (2)$$

Fluorine in the investigated system acts as a major to minor element, with its partitioning expected to be in the Raoult's law domain. We therefore discuss the exchange of fluorine between biotite and silicate melt in terms of exchange coefficients (Kd) rather than a Nernst partition coefficient (D);

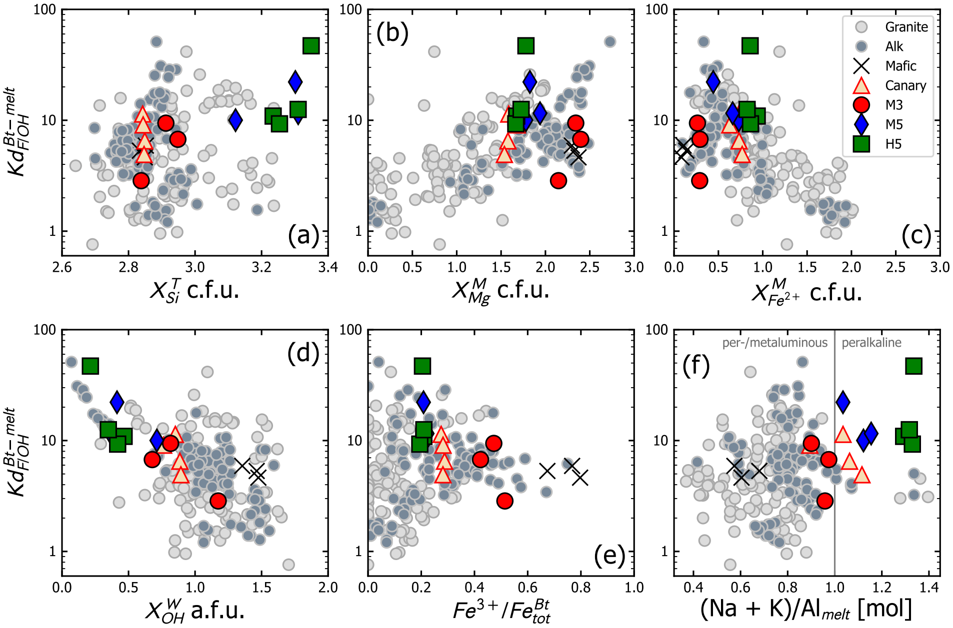

Figure 5 Biotite-melt fluorine/hydroxyl exchange coefficients vs. biotite and melt compositional parameters for our experiments and Canary Islands pyroclastic rocks, compared with literature experiments, labeled 'Granite', 'Alk', 'Mafic' (references are in Appendix B. a.f.u. is anions per formula unit, and c.f.u. cations, both of which are calculated for a total charge of 22 per formula unit following Li *et al.* (2020).

$$Kd_{\mathrm{F/OH}}^{Bt-melt} = (X_{F}^{Bt}/X_{\mathrm{OH}}^{Bt})/(X_{\mathrm{F}}^{melt}/X_{\mathrm{OH}}^{melt}) \tag{3}$$

where X_{F}^{Bt} and X_{OH}^{Bt} are mole fractions of F and OH on the biotite W site, and X_{F}^{melt} and X_{OH}^{melt} are mole fractions of F^- and OH^- in the silicate melt. A spreadsheet to calculate these terms is provided in Appendix B.

The $Kd_{\mathrm{F/OH}}^{Bt-melt}$ are 9.3–47.0 for our experiments, and 4.9–11.4 for the Canary Islands natural mineral-melt pairs (Fig. 5), ranges that are broadly consistent with literature experiments on granitic compositions (Icenhower & London 1997; 1.9–20.6), and on alkali-rich basalt to tephriphonolite compositions (Zhang *et al.* 2022; 6.1–51.1). This shows that F is compatible to highly compatible in biotite (for alkaline compositions in particular) and that if sufficient biotite is crystallising, it will deplete the residual melt of fluorine.

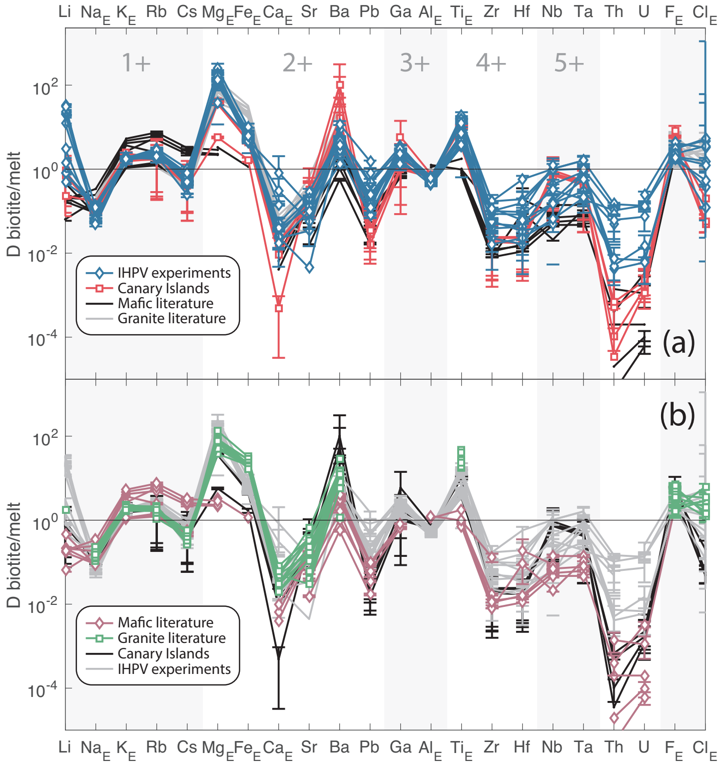

Figure 6 Biotite/melt element partition coefficients for experiments and Canary Islands pyroclastic rocks. Shown for comparison are published experimental partition coefficients for mafic compositions from Adam *et al.* (1993); LaTourrette *et al.* (1995); Schmidt *et al.* (1999); Green *et al.* (2000); Adam & Green (2006), and from granitic compositions from Icenhower & London (1995, 1997). Panel (a) and (b) show the same data in a different order and colour to aid readability. Elements with a subscript E are partition coefficients determined by EPMA (this study). All other D_i values determined for this study were measured by LA-ICP-MS.

In experiments containing greater concentrations of fluorine, the biotite are offset to higher Mg contents and lower Ti contents, indicating that the exchange mechanism (Eqn. 1) is driven to the left in biotite dominated by F rather than OH. This finding confirms that the Ti-in-biotite thermometer of Henry *et al.* (2005) should not be applied to fluorine-bearing systems since variations in fluorine content reduce the amount of Ti in biotite at a given Mg# and temperature, resulting in an over-prediction of temperature (also see Patiño Douce, 1993; Patiño Douce *et al.*, 1993; Li & Zhang, 2022).

Trace-element partitioning

Apparent Nernst partition coefficients (D values) are reported for twelve experimental and four Canary Islands biotite-glass pairs (Fig. 6, Table 4). D values are highly consistent among our experiments and

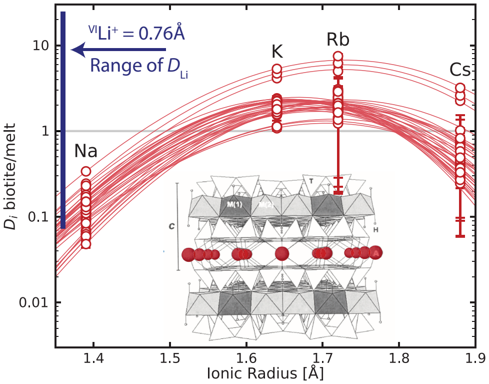

Figure 7 Onuma diagram for partitioning of 1+ cations between the mica ^{XII}A interlayer site and silicate melt (this study & literature). Note the range of D values for Li^{+}, which is too small for the A-site. Mica structure from Brigatti & Guggenheim (2002). See Figure S5 for a comparison to lattice site sizes determined via X-ray diffraction (Brigatti & Guggenheim, 2002).

are broadly similar to those reported from existing experiments on mafic or granitic compositions (Adam *et al.* 1993; Icenhower & London 1995; LaTourrette *et al.* 1995; Schmidt *et al.* 1999; Green *et al.* 2000; Adam & Green 2006).

Biotite/melt partition coefficients for the large R^{+} cations (Na, K, Rb, and Cs) cover a narrow range of values (Figs 6, S4), with K and Rb being compatible in biotite (D_{K} 1.43–2.67, D_{Rb} 1.74–3.08), and Na and Cs being incompatible to weakly compatible (D_{Na} 0.05–0.51, D_{Cs} 0.41–1.02). D values for these four monovalent ions define Onuma parabolae (Onuma *et al.*, 1968), consistent with their partitioning onto the twelve-fold coordinated A-site (interlayer) of biotite (Fig. 7). Increases to the fluorine content of the biotite subtly elevate partition coefficients for Rb while having little influence on the behaviour of Na, K and Cs (Fig. S4).

Lithium is weakly incompatible to strongly compatible in biotite, with D_{Li} values in our experiments and natural samples from 0.24–32.8 that are decoupled from those for larger R^{+} cations (Fig. 6). This decoupling results from the Li^{+} cation being too small for the XII A-site, and instead sitting in the octahedral M-sites of the biotite lattice ($^{\mathrm{VI}}\mathrm{Li} = 0.76$ Å; with M-site radii from X-ray diffraction on natural biotite = 0.50–0.86 Å; Brigatti & Guggenheim 2002, Fig. 7). Our apparent D_{Li} values overlap partly with compiled experimental studies on mafic and granitic compositions. There is excellent correspondence of D_{Li} between the Canaries samples and the M3 composition experimental charges (D_{Li} 0.24–0.90, Fig 8). Fluorine-rich experiments on the M5 and H5 compositions have strongly elevated D_{Li}

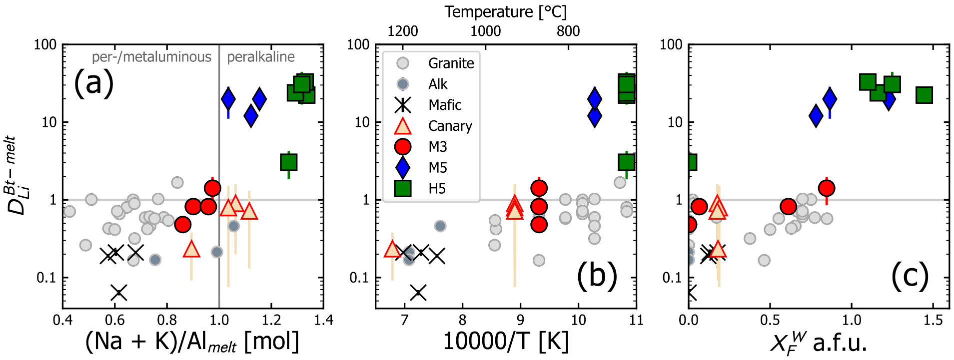

Figure 8 Biotite-melt D$_{Li}$ vs. biotite tetrahedral silica, inverse temperature and biotite fluorine content for our experiments and Canary Islands pyroclastic rocks, compared with compiled experiments from literature. 'Granite' compositions from Icenhower & London (1995); Evensen & London (2002); Pichavant *et al.* (2016); Horányi *et al.* (2025); 'Alk' compositions from Schmidt *et al.* (1999); 'Mafic' compositions from LaTourrette *et al.* (1995); Adam & Green (2006). Uncertainty on D$_{\mathrm{Li}}$ values is shown at the 1σ level. *a.f.u.* is anions per formula unit, and *c.f.u.* cations, both of which are calculated for a total charge of 22 per formula unit.

relative to the Canaries rocks and M3 composition experiments (Fig 8c; e.g., for M5 and H5 experiments with 1.25–2.5% bulk fluorine, D_{Li} is 12.0–32.8). Lithium D_{Li} values further show positive correlations with biotite X_{Si}^{T} and inverse temperature (Fig 8a,b).

The large R^{2+} cations Ca, Sr, Ba and Pb (residing on the biotite A-site) show a larger range of partitioning behaviour compared with R^{+} cations on this site. Their D values generally fall within the range of published experimental values for mafic and granitic compositions (Fig. 6). Ca is strongly incompatible in biotite (D_{Ca} 0.004–0.06), Sr and Pb are incompatible to weakly compatible (D_{Sr} 0.10–0.29, D_{Pb} 0.02–1.54) and Ba is compatible (D_{Ba} 1.3–11.8). This trend reflects the decreasing mismatch in radius between the ions and the biotite $^{\mathrm{XII}}$A site. D_{Ba} from our experiments and Canary Islands rocks define a negative log-linear correlation with inverse temperature (temperature based on phase equilibrium experiments of Andújar & Scaillet 2012; Fig. S3), which contrasts with the positive log-linear correlation reported by Wood & Blundy (2014). We attribute this mismatch to a smaller decrease in biotite solubility with increasing temperature (and hence A-site D_0^{2+}) in our alkali-rich compositions relative to those mafic and granitic data compiled by Wood & Blundy (2014). Calcium partition coefficients could not be calculated for all of our samples owing to low concentrations of Ca in the biotite and high LA-ICP-MS background counts for ^{44}Ca due to interferences from CO_2^{+} and N_2O^{+}.

The ions Ga^{3+} and Ti^{4+} are compatible in biotite (D_{Ga} 1.3–3.5, D_{Ti} 3.3–19.0, Fig. 6), whilst the 4+ and 5+ HFSE are incompatible to weakly compatible (D_{Zr} 0.02–0.17, D_{Nb} 0.05–1.2), and actinides U and Th are incompatible. This behaviour is similar to that in the compiled literature data (Fig. 6b).

The REE and Y are strongly incompatible, with the biotite usually containing concentrations of REE below the detection limit of our laser ablation setup (Fig. S2). Their partition coefficients are less than 10^{-2}. The REE^{3+} cations have ionic radii intermediate between the size of the M and A-sites of biotite (cf. Schmidt *et al.*, 1999), and their very low biotite/melt partition coefficients reflect this. Partition coefficients for La are highest as it has the smallest mismatch in radius with the A-site of biotite (our Canaries data and Adam & Green 2006, see Fig. S2).

Fits to the lattice strain model

The equilibrium partitioning of trace-elements between minerals and silicate melts is controlled largely by the size and elasticity of the crystal lattice sites (Onuma *et al.*, 1968; Brice, 1975; Blundy & Wood, 1994; Wood & Blundy, 2014) and the ability of the mineral to accommodate a local excess or deficit in charge (Blundy *et al.*, 1998; Mollo *et al.*, 2020). This behaviour is quantitatively described by the lattice-strain equation:

$$D_i^{min./melt} = D_0\ exp\left[\frac{-4\pi E_s N_a}{RT}\left(\frac{r_0}{2}(r_0 - r_i)^2 - \frac{1}{3}(r_0 - r_i)^3\right)\right] \tag{4}$$

where r_0 is the ideal radius for the lattice site (Å), E_s is its Young's modulus (i.e. stiffness in GPa), D_0 is the strain-free partition coefficient, N_a is Avagadro's number, R is the gas constant, T is temperature (Kelvin) and r_i is the ionic radius of each element (Å). The r_0 is controlled by mineral composition as the lattice site dimensions change systematically with, for example, $Mg^{2+} \rightleftharpoons Fe^{2+}$ exchange or $Al^{+3} \rightleftharpoons Si^{4+}$ substitution. The same is true for the elastic properties of the lattice, and hence E_s, and mineral solubility, which is tracked by D_0. Lattice strain parameters also vary with the physical conditions, for example via thermal expansion of the lattice with increasing temperature and its compression with increasing pressure. These trends can (in part) be estimated from independently obtained data, e.g., thermal expansion from high-temperature x-ray diffraction.

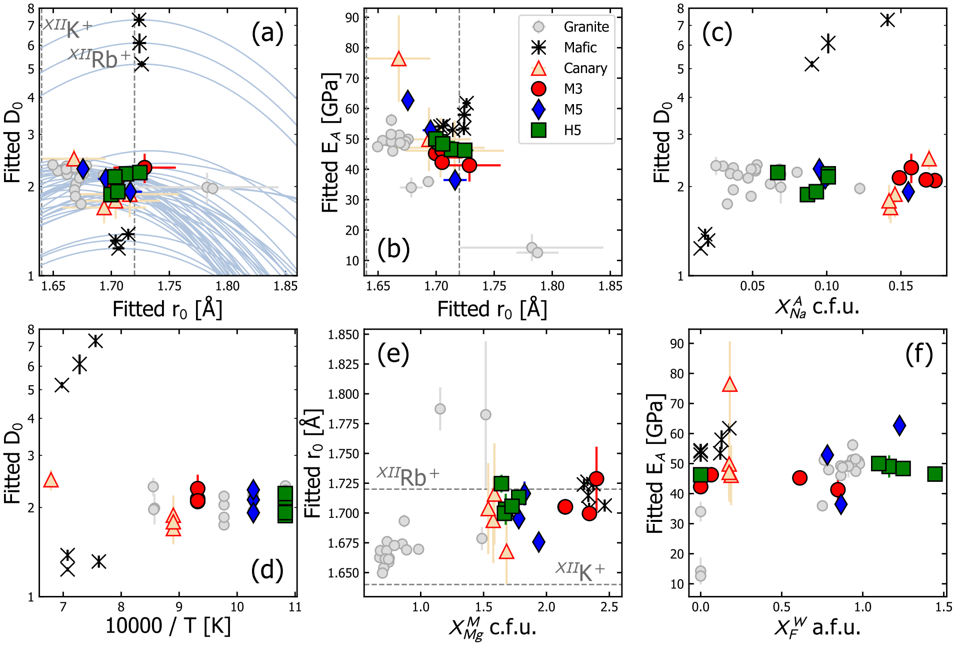

Figure 9 Lattice strain parameters for 1+ ions in the A-site of biotite, compared with our fits of published experimental partition coefficients for mafic systems (Adam *et al.*, 1993; LaTourrette *et al.*, 1995; Schmidt *et al.*, 1999; Green *et al.*, 2000; Adam & Green, 2006) and granitic compositions (Icenhower & London, 1995). (a) The latter have smaller A-site sizes (r_0) for a given D_0 than our samples and experiments performed with mafic compositions and (b) similar E$_A$ values. (c) D_0 shows a positive correlation with Na in biotite at Na contents $\leq$ 0.1 c.f.u., and (d) a positive correlation with inverse temperature. (e) r_0 vs. the X^M_{Mg} of biotite show a positive correlation, (f) E_A vs. X^W_F shows no clear correlation. Ionic radii after Shannon (1976). Uncertainty on all fitted lattice strain parameters is shown at the 1σ level. *a.f.u.* is anions per formula unit, and *c.f.u.* cations, both of which are calculated for a total charge of 22 per formula unit.

.

To investigate the systematics in D_i values and the mechanisms by which alkali elements are incorporated into biotite, element partitioning behaviour was explored using the lattice strain model. Parabolae for 1+ ions were fitted for the A-site (XII coordination) using the elements Na, K, Rb and Cs, with fits weighted based on analytical uncertainties on the partition coefficients (Fig. 7). For 1+ ions in twelvefold coordination, the data define r_0 values of 1.7–1.73 Å, E_s 35–75 GPa, and D_0 1.2–7.5. The r_0 parameter is similar for our experimental biotite, our natural Canaries biotite, and for biotite grown from mafic melts (Fig. 9). Biotite in granitic experiments has a smaller r_0 of 1.64–1.68 Å. A–O bond lengths determined for biotite via single-crystal X-ray diffraction are reported as inner and outer sphere values (Fleet, 2003). After subtraction of the ionic radius of tetrahedral O^{2-}, their A-site cation radii are 1.586–1.579 Å (median 1.587 Å) for the inner sphere, and 1.976–1.988 Å (median 1.980 Å) for the outer sphere; bracketing the range of r_0^{1+} values fitted to element partitioning data (Fig. 9).

The low Young's modulus values (35–75 GPa) for the A-site of biotite indicate its relative flexibility compared with the M2-site of clinopyroxene, or the cation site of plagioclase (cf. Wood & Blundy, 2014). These elastic modulii are similar to values measured for biotite using a spherical nanoindentation apparatus at room temperature (30.8–51.4 GPa, layer-normal; Lanin *et al.*, 2021).

D_0 values for 1+ ions at the A-site have a narrow range of positive values 1.2–7.5. A positive correlation exists between r_0^{1+} and D_0^{1+} for our experiments and for mafic compositions (Fig. 9a, Schmidt *et al.*, 1999; Adam & Green, 2006). No such correlation is observed for granitic experiments (Icenhower & London, 1995). As D_0^{+} tracks the solubility of an ideal monovalent cation in the biotite A-site (cf. Wood & Blundy, 2014), a similar chemical substitution may be related to expansion of the A-site (r_0) facilitating incorporation of 1+ ions.

Lattice strain fits were attempted for the large 2+ cations onto the A-site (Ca, Sr, Ba), but generation of a satisfactory parabola was not possible in most cases owing to the low concentrations of Ca in biotite, and corresponding high analytical uncertainty. Fits with Pb were attempted, but Pb plotted consistently below lattice strain parabolae defined by the other three elements, an effect reported elsewhere and attributed to the non-ideal electronic structure of the Pb^{2+} ion (Wood & Blundy, 2014).

The 4+ and 5+ HFSE ions Ti, Zr, Hf, Nb, and Ti provide an insufficient spread of radii for the fitting of lattice strain parabolae for the two M-sites in biotite.

Empirical element partitioning models

The partitioning behaviour of major- and trace-elements between minerals and melts varies systematically with the physicochemical conditions of magmas (Wood & Blundy, 2003). In principle, partitioning behaviour can be predicted a-priori from the dependence of the lattice-strain parameters r_0, D_0 and E_s on pressure, temperature and the composition of the mineral and the melt. A number of empirical models have been presented that describe element partitioning between melt and various minerals (e.g., Wood & Blundy 1997; Bédard 2014, 2023; Sievwright *et al.* 2017; Sun *et al.* 2017; Beard *et al.* 2019, 2020; Mollo *et al.* 2020). These models permit forward modelling of the major- and trace-element budget of crystallising magmatic systems and vice versa can be used to read the mineral record of melt composition in natural volcanic and intrusive igneous systems (cf. van Hinsberg *et al.* 2010).

Few models so far pertain to biotite-melt element partitioning (e.g., Zhang *et al.*, 2022) and none, to our knowledge, are calibrated for compositions extending to peralkaline magmatic systems. We present six models: one describes the F-OH exchange between silicate melt and the biotite W-site; a second, based on lattice strain theory, describes the exchange of 1+ cations between silicate melt and the ^{XII}A-site of biotite; a third, fourth and fifth describe lithium partitioning between the melt and the M-sites of biotite (with and without a temperature term, and without a fluorine term) and finally a sixth addresses niobium. Model performance is shown in Figures 10–11, coefficients are in Table 5 and an EXCEL spreadsheet of the empirical partitioning models is provided in Appendix B.

Our calibration database includes 229 biotite-melt partitioning experiments and covers a wide range of melt and biotite composition, pressure, temperature, and oxygen fugacity (50–3000 MPa, 620–1200 °C, log fO_2 = IW (iron-wüstite) to MH (magnetite-haematite) ≈ ΔFMQ -5 to +5). The database includes experiments with a range of bulk compositions including our tephrite to phonolite composition experiments, alkali basalt to trachyte Zhang *et al.* (2022), peraluminous and metaluminous granite (Icenhower & London, 1995, 1997), and nepheline-normative basanite (Adam & Green, 2006). A full list of references is in Appendix B. Experiment biotite have 2.6–3.3 ^{T}Si, 0–1.4 ^{M}Al, 0–2.7 ^{M}Mg and 0–1.8 ^{W}F ions per formula unit (total unit charge of 22). Quenched melt has 44.7–78.3 wt% SiO_2, 0–1.0 molar Mg/(Mg + Fe), and 0.37–1.40 molar (Na + K)/Al. The majority of trace-element partition coefficients in this data set were determined via SIMS or LA-ICP-MS analyses, minimising analytical uncertainty compared to data from electron microprobe.

A model for F-OH exchange between silicate melt and the biotite W-site

To determine the principal physicochemical controls on the exchange of F and OH anions between silicate melt and the W-site of biotite a least-squares multiple linear regression analysis was performed using our new $Kd^{\text{Bt-melt}}_{\text{F/OH}}$ values, alongside a compilation of previously published experimental data. Candidate fitting parameters were initially examined in binary scatter diagrams (e.g., Fig. 5) to check for covariance and to ascertain whether correlations were linear. Intensive variables for multiple linear regression models for $Kd^{\text{Bt-melt}}_{\text{F/OH}}$ were introduced following a hierarchical forward selection criterion with switching. Only parameters with student t-tests showing statistical significance at the 95% confidence level were retained, with the preferred model incorporating five biotite compositional terms (Table 5). Uncertainties on the model coefficients were determined via bootstrapping. The PRESS R^2 value obtained by repeated random sub-sampling of the data set is similar to the R^2 value calculated for the full data set, indicating that the model is robust and has high predictive power. Full regression reports are in Appendix D.

The final set of significant parameters defines the model equation:

$$\begin{aligned} LnKd^{\text{Bt-melt}}_{\text{F/OH}} &= a_1 + a_2 X^T_{\text{Si}} + a_3 X^M_{\text{Mg}} + a_4 X^W_{\text{OH}} \\ &+ a_5 X^M_{\text{Fe}^{2+}} + a_6 \text{Fe}^{3+}/\text{Fe}^{Bt}_{tot} \end{aligned} \tag{5}$$

Compositional coefficients are included for the T, M and W sites of the biotite structure, and for the oxidation state of iron in the biotite (Table 5). The positive X^T_{Si} coefficient is consistent with Pearson acid-base theory: The W and T sites are adjacent in the biotite lattice, meaning there is a direct bond between Al or Si in the T site and OH or F in the W site (Munoz, 1984; Brigatti & Guggenheim, 2002). Si^{4+} has a higher Z/r relative to Al^{3+}, therefore is expected to bond preferentially with F^-, which has a higher electronegativity than OH^-. The positive correlation between X^M_{Mg} and $Kd^{\text{Bt-melt}}_{\text{F/OH}}$ and negative correlation with $\text{Fe}^{3+}/\text{Fe}^{\text{Bt}}_{\text{tot}}$ and $X^M_{\text{Fe}^{2+}}$ are consistent with Fe^{2+}–F avoidance in silicate minerals (Rosenberg & Foit, 1977; Munoz, 1984; Finch *et al.*, 1995; Fleet, 2003), a phenomenon attributed to crystal field theory. The negative correlation between $Kd^{\text{Bt-melt}}_{\text{F/OH}}$ and biotite X^W_{OH} might result from non-ideal mixing of OH^- and F^- on the biotite W-site, or in the silicate melt.

As model equation 5 includes biotite compositional terms only it can be applied to biotite grains from natural igneous systems where one cannot directly determine melt composition, and the pressure and temperature of equilibration. The multiple linear regression procedure did not identify temperature, pressure or melt compositional terms as strong predictors for F/OH exchange, relative to the biotite compositional parameters shown above.

An empirical model to predict F/OH exchange between biotite and melt was recently presented by Zhang *et al.* (2022), and was calibrated using experiments on alkaline-silicate bulk compositions, though most were not peralkaline (grey circles on Fig. 5e). On a measured vs. predicted diagram (Fig. 10d), we note that the Zhang *et al.* (2022) model accurately reproduces some of our calibration data set; for example Kd values for our experiments with peralkaline bulk compositions are predicted to within a factor of 2–3 of measured values. However, the Zhang model systematically under-estimates $Kd^{\text{Bt-melt}}_{\text{F/OH}}$ values for some peraluminous granite experiments (e.g., Icenhower & London 1995) and for our Canary

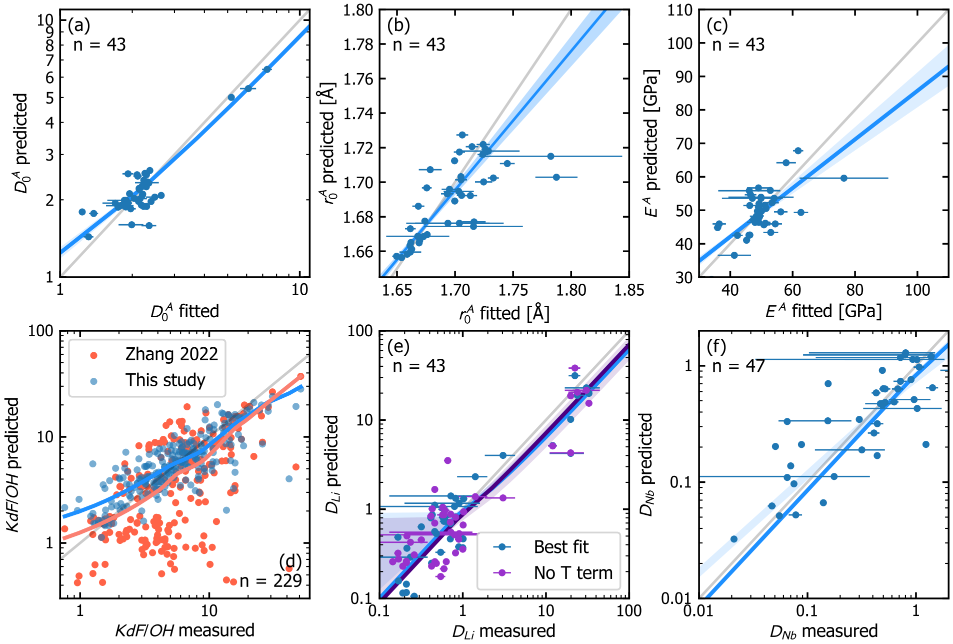

Figure 10 Fitted (or measured) vs. predicted model values for (a-c) lattice strain parameters describing partitioning of 1+ cations between the A-site of biotite and silicate melt, (d) F-OH exchange, (e, f) Li & Nb partition coefficients. Model equations are in the main text, with coefficients given in Table 5. Grey lines show 1:1 relationships. Blue and purple coloured lines are robust linear regressions, except for in (b) where the fit is a weighted least-squares based on precision, and in (d) where regression lines are locally-weighted scatterplot smoothing (LOWESS) fits. Shaded 68.2% confidence intervals ($\sim 1\sigma$) were generated via bootstrapping.

Islands natural biotite-melt pairs, in extreme cases by over an order of magnitude (Figs 10d, S7a). The peraluminous granite experiments of Icenhower & London (1995) have much higher ASI values (mean 1.76) of the melt) than the calibration data set for the model of Zhang *et al.* (2022)(1.17), which may be why their model predicts such low $Kd^{\text{Bt-melt}}_{\text{F/OH}}$ values for these compositions.

A partitioning model for 1+ ions at the biotite A-site

The partitioning of 1+ cations between silicate melt and the A-site of biotite is described below using empirical models to predict the lattice strain parameters r_0^+, D_0^+ and E_s^+ as a function of pressure, temperature and composition. Firstly, we fitted Onuma curves for the monovalent ions Na–Cs, with weighting based on analytical precision on the experimental and literature reported D values. Uncertainty on the fits was determined via bootstrapping. Where precision on biotite or glass analyses was not reported (e.g., Evensen & London 2002) we attempted fits using uncertainty determined on

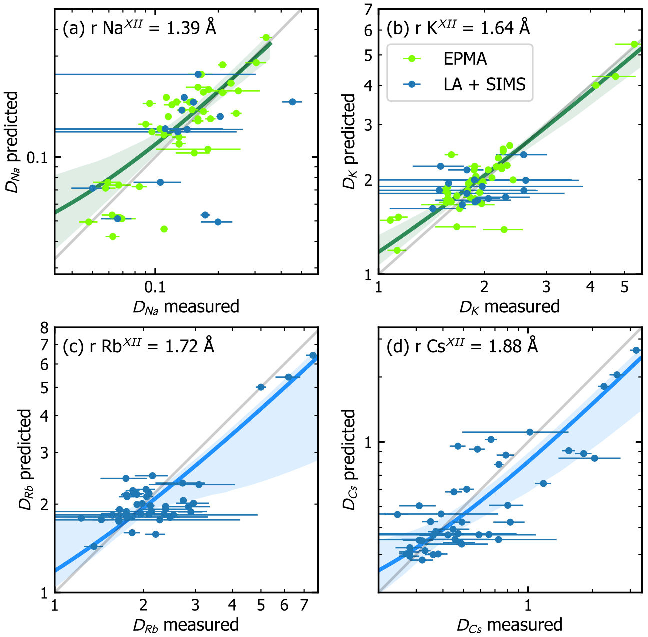

Figure 11 Measured vs. predicted D values for $1+$ between silicate melt and the XII-coordinated biotite A-site. Grey lines are 1:1 fits. Coloured robust regression lines with shaded 95% confidence intervals ($\sim 2\sigma$) were generated via bootstrapping (green use EPMA data, blue use LA-ICP-MS or SIMS data)

.

other charges from the same study (see Appendix B). For several experiments from the literature compilation, D values for one or more ions fell outside the 95% confidence interval on the LST parabola. We do not consider these charges further as we suspect issues with either the analytical or experimental procedure. Onuma curves for each experiment, and histograms showing LST parameters determined via bootstrapping are given in Appendix D.

Lattice strain parameters for 43 experiments were used to fit empirical models that describe partitioning of the monovalent ions Na–Cs. A least-squares multiple linear regression analysis was performed following the method described above for F-OH exchange. The largest number of significant terms was five for the E^{+} parameter (Table 5). Equations from the multiple linear regression are given below:

$$\begin{aligned} \mathrm{Ln}D_0^{A+} &= b_1 + b_2 X_{\mathrm{Na}}^{A} + b_3 \mathrm{NBO/T}^{melt} \\ &+ b_4 (\mathrm{Na} + \mathrm{K})/\mathrm{Al}^{melt} + b_5 \times 10^4/\mathrm{T[K]} \end{aligned} \tag{6}$$

$$r_0^{A+} = b_6 + b_7 X_{\mathrm{Fe^{2+}}}^{M} + b_8 X_{\mathrm{Mg}}^{M} + b_9 X_{\mathrm{Ti}}^{M} + b_{10} X_{\mathrm{F}}^{W} \tag{7}$$

$$\begin{aligned} E^{A+} &= b_{11} + b_{12} X_{\mathrm{K}}^{A} + b_{13} \mathrm{Fe}^{3+}/\mathrm{Fe}_{tot}^{Bt} \\ &+ b_{14} X_{\mathrm{Fe^{3+}}}^{M} + b_{15} X_{\mathrm{Ti}}^{M} + b_{16} X_{\mathrm{O^{2-}}}^{W} \end{aligned} \tag{8}$$

where b_i are the regression coefficients for each variable (Table 5) T is temperature in Kelvin and P is pressure in MPa. The resultant empirical models account well for changes to the lattice-strain parameters over a range of compositions from basanite to peralkaline phonolite to peraluminous granite, reproducing the larger r_0 for the interlayer site typical for biotite grown from sodic alkaline silicate melt (Fig. 9b). PRESS R^2 values are similar to overall R^2 values, indicating that the models are robust and have high predictive power. Fitted vs. predicted diagrams for the lattice strain parameters are in Figure 10a–c, and full multiple regression reports are in Appendix D.

The model for $\mathrm{Ln}D_0^{A+}$ includes a compositional term from the A-site of biotite, two melt compositional terms, and a term for inverse temperature. The positive correlation between A-site Na and D_0^{A+} is the largest contribution to the model, indicating that elevated concentrations of large ions other than K on the interlayer site (e.g., Na, Ca, Ba) are associated with higher values of D_0^{A+}. The relationship between D_0^{A+} and the melt compositional terms NBO/T (non-bonding oxygens per tetrahedral cation; i.e., the degree of melt depolymerisation; Mills 1993) and the molar (Na + K)/Al ratio, and with inverse temperature are tied to the solubility of the mineral in the melt (Wood & Blundy, 2003). These terms are physically grounded as they are consistent with increased stabilisation of biotite in systems with a depolymerised melt structure (with high volatile and alkali content), and at low temperature.

The model for r_0^{A+} incorporates compositional controls on the M and W sites of biotite. Model fitting was performed with weights for each experiment assigned by $r_{0,\mathrm{weight}}^{A+} = 1/(r_{0,\sigma}^{A+}/r_0^{A+})^2$. For this reason the model reproduces more accurately the r_0 for experiments where r_0 fits have been determined to higher precision (Fig 10b). While our r_0^+ model has a lower predictive power than our D_0^+ and E^+ models it still has physical grounding: The positive $^{\mathrm{M}}$Mg and $^{\mathrm{M}}$Fe^{2+} terms, and a negative $^{\mathrm{M}}$Ti term, are consistent with a larger interlayer separation, as determined via X-ray diffraction, in Mg-rich micas relative to Ti-rich ones (Brigatti & Guggenheim 2002, Fig. S5). The model also contains a small negative contribution from $^{\mathrm{W}}$F, which has a small effective ionic radius relative to hydroxyl anions it substitutes for.

The model for E_A^+ has compositional terms from the A, M and W sites of biotite, as well as the iron oxidation state in biotite. The negative $^{\mathrm{A}}$K term suggests that the interlayer of K-rich micas is less stiff than those with higher proportions of smaller, and perhaps less readily deformed, Na$^+$ ions. The compositional term X_{Ti}^M is positively correlated with E_A, whereas X_{O}^W has a strong negative correlation. The polarity of these terms are physically grounded, as Ti^{4+} is a small ion that form bonds that are not as readily deformed, compared to bonds including larger Mg and Fe cations. Similarly, the large O^{2-} anion will form relatively less stiff bonds than the smaller W-site F$^-$ and OH$^-$ anions that it subsitutes for.

Diagrams of measured vs. predicted D values for individual R$^+$ cations are given in Figure 11. For the A site all of the measured R$^+$ partition coefficients, except for Na$^+$, are reproduced to better than a factor two. D values for the elements K and Rb are reproduced most faithfully because their XII-coordinated ionic radius is closer to the biotite r_0^A and therefore prediction of their partitioning behaviour is influenced less strongly by inaccuracies in predicted E_A values. Partitioning behaviour for Na is not predicted accurately by our lattice strain model, with the lowest measured D_{Na} values being underpredicted (Fig. 9a). As the effect is of similar magnitude for EPMA and higher-precision LA and SIMS measurements this bias is unlikely to be an analytical artefact. It may reflect incorporation of a small amount of Na cations on the biotite M sites.

Three models for lithium partitioning

Using the methodology described above, we fitted three empirical models that describe the partitioning behaviour of Li between silicate melt and the M-sites of biotite. The same training data set described above was used, with 43 entries for lithium. Partitioning was explored directly, rather than in the frame of lattice strain theory, owing to the lack of other 1+ cations with radii similar to the biotite M-sites. The *'Best fit'* equation for the partitioning of lithium, as obtained from multiple linear regression, is given below:

$$\mathrm{Ln}D_{\mathrm{Li}} = c_1 + c_2(\mathrm{Na}+\mathrm{K})/\mathrm{Al}^{melt} + c_3 \times 10^4/\mathrm{T[K]} + c_4 X_{\mathrm{F}}^{W} \tag{9}$$

where c_i are the regression coefficients for each variable (Table 5). Measured vs. predicted D_{Li} values are shown in Figures 10e and S8.

The first model for D_{Li} includes one melt composition term, a term for inverse temperature, and a term for biotite composition and reproduces accurately the two order of magnitude range of D_{Li} values in the training data set (Fig. 10e; S8). The positive $(\mathrm{Na}+\mathrm{K})/\mathrm{Al}^{melt}$ term is consistent with the low whole-rock lithium content of peralkaline magmatic rocks (e.g., Teng *et al.* 2009), and the association between lithium-caesium-tantalum pegmatites and peraluminous granites (Gardiner *et al.*, 2024). The positive correlation between D_{Li} and inverse temperature likely results from broad variations in melt and mineral composition that are correlated with temperature. It is consistent with the observation that F-Li rich micas form at low temperatures in evolved granitic systems (Förster *et al.*, 1999; Černý *et al.*, 2005) and that silicate minerals from slowly-cooled alkaline and calc-alkaline lavas and ignimbrites are enriched in Li relative to rapidly cooled portions of the same volcanic deposits (Neukampf *et al.*, 2023). Correlations between the fluorine and lithium content of micas are widely reported from rare metal granites, pegmatites, and metamorphic rocks (Martins *et al.*, 2012; Kunz *et al.*, 2022; Breiter *et al.*, 2023).

A second temperature-free model for lithium partitioning was calibrated, as when interrogating minerals from natural systems, the temperature of equilibration and melt composition can be challenging to constrain. The above procedure was used, but only biotite compositional terms were included in the list of permitted intensive variables. The temperature- and melt-free equation for the partitioning of lithium is as follows:

$$\mathrm{Ln}D_{\mathrm{Li}} = c_5 + c_6 X^{M}_{\mathrm{Fe}^{2+}} + c_7 X^{M}_{\mathrm{Mg}} + c_8 X^{T}_{\mathrm{Si}} \tag{10}$$

The predictive power of the temperature-free model for lithium partitioning is slightly weaker than that our 'best fit' model ($R^2 = 0.799$ vs. 0.859), but reproduces all measured and compiled D_{Li} values to within a factor of two (Fig. 10e, S8). The fit coefficients are physically grounded: Mg^{2+} & Fe^{2+} have relatively low charge compared to Fe^{3+} and Ti^{4+} and their positive fit coefficients indicate their relative readiness to substitute for Li^{+}. Additionally, increasing the Si^{4+} content of the T-site of biotite over Al^{3+} may promote incorporation of Li^{+} in place of more highly-charged M-site cations such as Mg^{2+}, Fe^{2+} and Ti^{4+} (cf. Breiter *et al.* 2023).

A third empirical biotite partitioning model is designed for integration directly with the current generation of phase equilibrium model systems that do not include fluorine (e.g., MELTS family, HPx-eos; as implemented in Gibbs energy minimisation software such as THERMOCALC, and MAGEMin; Ghiorso *et al.* 2002; Asimow *et al.* 2004; Gualda *et al.* 2012; Weller *et al.* 2024; Green *et al.* 2025). For this reason, our best-fit model cannot currently be applied to forward model lithium behaviour in silicate magmatic systems. Instead, we recommend using the following empirical relationship:

$$\begin{aligned}\mathrm{Ln}D_{\mathrm{Li}} = c_9 + c_{10} X^{M}_{\mathrm{Fe}^{3+}} + c_{11}(\mathrm{Na}+\mathrm{K})/\mathrm{Al}^{melt} \\ + c_{12} 10^4/T[K]\end{aligned} \tag{11}$$

The predictive power of this fluorine-free model for lithium partitioning is intermediate between that of our 'best fit' model and temperature-free model ($R^2 = 0.840$ vs. 0.799 & 0.859; Table 5). The fit coefficients in model 11 are physically grounded, with a negative $X^{M}_{\mathrm{Fe}^{3+}}$ term tracking an increasingly positive charge of the biotite M-site, and corresponding increased difficulty of incorporating monovalent Li^{+} cations. The positive $(\mathrm{Na}+\mathrm{K})/\mathrm{Al}^{melt}$ & $10^4/T$ coefficients follow mechanisms discussed for our best fit model (Equation 9) above.

A model for niobium partitioning

We fitted an empirical model to describe Nb partitioning between biotite and silicate melt. The D_{Nb} model has physical grounding with a compositional term for the M-sites of biotite, and an inverse temperature term:

$$\begin{aligned} \mathrm{Ln}D_{\mathrm{Nb}} = d_1 + d_2 X^{M}_{\mathrm{Fe}^{2+}} + d_3 X^{M}_{\mathrm{Mg}} + d_4 \mathrm{NBO/T}^{melt} \\ + d_5 \mathrm{P[MPa]} \end{aligned} \tag{12}$$

The coefficients d_2 and d_3 describe a negative correlation between Nb^{5+} incorporation in biotite and the Fe^{2+} and Mg content of biotite. The substitution of Nb^{5+} for Fe^{2+} or Mg^{2+} incurs a charge penalty of 3+ that must be balanced elsewhere within the biotite structure, a larger penalty than if Nb replaced Fe^{3+} or Ti^{4+}. The positive correlation between D_{Nb} and melt NBO/T suggests that Nb activity in the silicate melt might rise with increasing depolymerisation of the silicate melt. However, this finding is reverse to that of Aseri *et al.* (2015) who report increases to solubility of HFSE oxide and silicate minerals with increasing melt alkalinity. We suggest the correlation incorporated into our model reflects broad variation activity of Nb in the silicate melt as well as that of biotite composition, which across our calibration data set may be stronger than the melt activity effect alone. The subtle negative correlation with pressure also likely results from broad correlations with melt and mineral composition. A second model fit was attempted where no melt, pressure or temperature terms were permitted to facilitate application to biotite grains from natural systems. However, a satisfactory fit was not possible.

Implications for mineralisation of Li and REE-HFSE in magmatic systems

Biotite has the highest lithium concentration of rock-forming mineral phases in both alkaline and calc-alkaline volcanic rocks globally (Ellis *et al.*, 2022; Neukampf *et al.*, 2023), and represents an important reservoir for lithium in metamorphic and plutonic environments (e.g., Kunz *et al.* 2022; Gardiner *et al.* 2024). Together, this indicates that biotite-melt partitioning is a major control on the lithium budget of many evolved crustal magmas. We note a wide range of partitioning behaviour for lithium that spans incompatible to strongly compatible behaviour (Fig. 8). The composition of biotite in residua generated during crustal melting, and the composition of biotite generated during subsequent crystallisation of silicate melts therefore has a strong influence on the lithium budget of magmas. Ultimately, element budgets control the ability of igneous systems to develop economic concentrations of metals, for example in lithium-caesium-tantalum pegmatites (e.g., Linnen *et al.* 2012; London 2018; Breasley *et al.* 2024; Koopmans *et al.* 2024; Goodenough *et al.* 2025; Wu *et al.* 2025).

First, we note a positive correlation between D_{Li} and inverse temperature (Fig. 8b). During progressive heating and melt extraction from crustal rocks (e.g., Loiselle & Wones 1979), this would initially produce a residual mineral assemblage containing Li-rich biotite, with a Li-poor silicate melt, a scenario consistent with field observations that Li and F-rich pegmatites are often notably younger than spatially associated granites (Simons *et al.*, 2016; Gardiner *et al.*, 2024).

A granite chronology of increasing Li abundance is also easier to explain if the effect of fluorine is considered: Fluorine can stabilise biotite to higher temperatures (Munoz, 1984; Peterson *et al.*, 1991), and is positively correlated with D_{Li} (Fig. 8c), therefore emphasises the temperature effect described above. Progressive melting of a fluorinated metasediment or granitoid precursor could therefore stabilise in the residual mineral assemblage biotite that becomes more fluorine-rich with an increasing degree of melt extraction (Finch & Tomkins, 2017). Multi-stage melt extraction (from an individual source volume) and eventual heating to F-biotite-out would release a Li and F-enriched silicate melt (cf. Morris *et al.* 2026, accepted). Such a mechanism provides a possible origin for LCT pegmatites contrasting with that of Koopmans *et al.* (2024) where granites derived from metasedimentary rock anatexis are themselves remelted.

Fractional crystallisation is also important for enriching incompatible trace-elements in magmatic systems. Because biotite-melt D_{Li} values are positively correlated with the molar (Na + K)/Al ratio of silicate melt (Fig. 8a), the residual enrichment of Li should be most efficient during crystallisation of magmatic systems with high Al/Si ratios. Such a model is compatible with the association between lithium-caesium-tantalum (LCT) pegmatites and peraluminous granites (Linnen *et al.*, 2012; London, 2018; Gardiner *et al.*, 2024). By contrast biotite crystallisation in peralkaline systems (high (Na + K)/Al) would efficiently deplete the residual melt of lithium.

Our results also have implications for REE-HFSE mineralisation in alkaline-silicate (and associated carbonatite) intrusions. Biotite is a major host of fluorine in evolved muscovite and fluorite-free igneous rocks (Speer, 1984; Finch *et al.*, 1995), and fluorine affects REE-HFSE behaviour. Synchrotron experiments on silicate melt structure resolve REE-F complexes (Ponader & Brown Jr., 1989), and an effect of fluorine on the medium-range structural environment around HFSE^{4+} cations (Farges, 1996). Both phenomena reduce the activity of these cations, and thus hinder their incorporation into minerals (Beard *et al.*, 2020; Xue *et al.*, 2024). Fluorine therefore promotes the residual enrichment of REE and HFSE^{4+} during crystallisation of both alkaline-silicate and carbonatite magmas.

To quantify the fluorine budget of evolved silicate magmas, we constrained the physicochemical controls on the exchange of hydroxyl and fluoride anions between biotite and silicate melt. Biotite can then be used as a mineral record or 'probe' for the fluorine content of the melts from which it formed, as has been calibrated for apatite (cf. McCubbin *et al.*, 2015; Riker *et al.*, 2018; Li & Costa, 2020). The range of $Kd^{Bt-melt}_{\mathrm{F/OH}}$ values across our new dataset and that compiled from experimental studies is ∼0.76–51.10. Where $Kd^{Bt-melt}_{\mathrm{F/OH}}$ values are high, crystallisation of even a small amount of biotite can effectively strip fluorine from the melt. This scenario occurs where biotite has high Si and Mg, and low Fe^{2+} and $\mathrm{Fe}^{3+}/\mathrm{Fe}_{\mathrm{tot}}$ ratios (Fig. 5). The same concepts hold for apatite, where F-OH exchange coefficients vary in the range ∼3–500 (Riker *et al.* 2018). In silica-undersaturated peralkaline systems, such as those associated with REE-HFSE mineralisation, the Fe/Mg ratio is commonly high. Biotite-melt $Kd_{\mathrm{F/OH}}$ values should therefore be low, facilitating residual enrichment of fluorine during crystallisation. Here, variations in biotite mode represents a major control on the fluorine concentration of residual melts.

Glimmerite, a biotite-rich rock formed through interaction between silicate or carbonate melts and their host rocks (O'Brien *et al.*, 2015; Giebel *et al.*, 2019; Vasyukova & Williams-Jones, 2022; Anenburg & Walters, 2024), therefore represents a potential trap for REE. By drawing down the fluorine concentration of the melt, massive crystallisation of biotite increases the activity of REE, which can trigger saturation of REE mineral phases. This may have occured at the Longbaoshan prospect, China, where multiple stages of metasomatism formed glimmerite containing an assemblage with the REE-bearing minerals chevkinite-(Ce), fluoroapatite, fluorobritholite-(Ce), synchysite-(Ce) and parisite-(Ce) (Yang *et al.*, 2025). Similar processes may occur during formation of glimmerite (or PIC: phlogopite, ilmenite, clinopyroxene) veins in the lithospheric mantle (e.g., Fitzpayne *et al.* 2018; Tappe *et al.* 2025).

Conclusions and possible applications

Twelve IHPV crystallisation experiments and four natural biotite-glass pairs from Tenerife, Canary Islands were used to constrain biotite-melt partitioning of minor- and trace-elements in sodic alkali-rich magmas and together with a compilation from the literature, constrain empirical models to predict F-OH exchange; partitioning of the monovalent ions Li, Na, K, Rb, Cs; and Nb partitioning over a broad range of silicate magmatic systems.

Our fluorine-bearing charges contain biotite offset to higher Mg and lower Ti content relative to equivalent fluorine-free experiments. This finding confirms that the Ti-in-biotite thermometer of Henry *et al.* (2005) is not calibrated for use in fluorine-bearing systems.

Most minor- and trace-elements are incompatible in biotite with the exception of Rb, Ba, Ga, Ti, and in Si-F-rich biotite, Li. The LIL elements Na, Cs, Sr and Pb, and HFS elements Zr, Hf, Nb and Ta are incompatible to weakly compatible (D_i = 0.008–1.6), whereas the REE, Y and actinides U and Th are strongly incompatible ($D_i \approx$ 0.0001–0.01).

To facilitate application of partition coefficients across a wide range of P-T-X conditions, we calibrated empirical models that describe partitioning with continuous functions, rather than as discrete points. Empirical models for F-OH exchange show preferential uptake of fluorine into Mg-rich biotite with high $^{\mathrm{T}}$Si and low Fe^{2+}. Biotite grown from evolved, Mg-poor peralkaline magmatic systems have a weaker preference for fluorine, therefore are predisposed to develop melts with high fluorine/water ratios during fractional crystallisation of a biotite-bearing assemblage. As fluorine and the REE have strong chemical interactions, the residual enrichment of F promotes the residual enrichment of REE.

Our empirical models for D_{Li} show a large positive correlation with biotite fluorine content and with melt alkalinity. As fluorine stabilises biotite to higher temperature the progressive melting of crustal rocks, for example during orogenesis, will eventually release F and Li together during a biotite-out reaction. Once in the melt, lithium can be enriched or depleted by crystallisation. In peraluminous systems the biotite has a low affinity for lithium, therefore evolved peraluminous granites are most likely to develop high concentrations of lithium.

Partition coefficients for the large 1+ cations Na–Cs define Onuma parabolae with r_0 and E_s values consistent with independent estimates from XRD and nanoindentation studies for the $^{\mathrm{XII}}$A-site. A further empirical model, based on lattice strain theory, can be used to determine partition coefficients for large 1+ cations over a wide range of P-T-X. For convenience we provide an EXCEL spreadsheet of the empirical partitioning models (Appendix B).

New constraints on element partitioning between biotite and melt may be used to forward model the crystallisation of magmatic systems and test mechanisms for the petrogenesis of mineral deposits, including for Li-bearing pegmatites and alkaline-silicate associated REE and HFSE mineralisation. Phase equilibrium modelling tools (e.g., Ghiorso & Sack 1995; Holland & Powell 2011; Holland *et al.* 2018; Heinonen *et al.* 2020; Riel *et al.* 2022; Weller *et al.* 2024; Green *et al.* 2025) can be coupled with empirical models that describe the saturation behaviour of accessory phases, facilitating modelling of various key elements outside of the model system used for activity-composition relations (cf. Yakymchuk *et al.* 2017). A similar approach, layering distribution coefficients between melt and major minerals permits forward modelling of the halogen, volatile, and trace-element budgets of magmatic systems across P-T-X space (Humphreys *et al.*, 2021; Nathwani *et al.*, 2023; Soderman *et al.*, 2025).

Our partitioning models also facilitate the interrogation of mineral grains, with or without compositional zoning, from natural igneous systems to determine the concentration of trace-elements in their parental melts (cf. Bédard 2001). By combining biotite/melt partition coefficients with our recent studies of clinopyroxene/melt element partitioning (Beard *et al.*, 2019, 2020), one can determine the concentration of a broad range of geologically important trace-elements in the parental melts for silicate-dominated magmatic systems.

Author contributions

CDB, VJvH and JS conceived the experiments, CDB conducted the experiments, wrote the first draft of the manuscript, analysed the results, fitted the models and prepared the figures. JHB contributed part of the compiled literature data set. All authors discussed the implications, edited and reviewed the manuscript.

Data availability

Major- (EPMA) and trace-element determinations (LA-ICP-MS) that underpin this study, along with data treatment procedures and empirical element partitioning models are provided in the Supplementary material. The data are further available at the GFZ data repository `https://doi.org/10.5880/fidgeo.2025.073`.

Acknowledgements

We thank the Geo.X partners GFZ & Universität Potsdam for access to the HP-GeoMatS Lab, Max Wilke, Hans Peter Nabein, Eleanor Berryman, Maria Stuff & Julia Pohlenz for assistance with HP experimental equipment, Lang Shi & Glenn Poirier for assistance with electron probe analyses, & Anna Jung for assistance with laser ICP-MS analyses. The manuscript benefited from discussions with Longbo Yang, Adrian Finch, Julia Neukampf, Tania Martins, Bob Linnen, Matt Morris, Marie Edmonds, and Nicolas Riel. We thank three anonymous reviewers for their encouraging and insightful reviews, and the journal editors Julia Hammer and Georg Zellmer for deftly handling this manuscript. This work was funded by PhD scholarships to CDB from Geotop, DIVEX, and the SEG Canada Foundation, and operating grants to VJvH and JS from the Natural Sciences and Engineering Research Council of Canada (grant numbers RGPIN-2014-05955, RGPAS-462335-2014) and the FQRNT team research project program. CDB, OMW, and CRS were supported by UKRI Future Leaders Fellowship grant MR/V02292X/1 to OMW.

References

Abdel-Rahman, A. F. M. (1994). Nature of biotites from alkaline, calc-alkaline, and peraluminous magmas. *Journal of Petrology*, *35*(2), 525–541.

Ablay, G. J., Ernst, G. G. J., Marti, J., & Sparks, R. S. J. (1995). The ∼2 ka subplinian eruption of Montaña Blanca, Tenerife. *Bulletin of Volcanology*, *57*(5), 337–355.

Adam, J. & Green, T. (2006). Trace element partitioning between mica- and amphibole-bearing garnet lherzolite and hydrous basanitic melt: 1. Experimental results and the investigation of controls on partitioning behaviour. *Contributions to Mineralogy and Petrology*, *152*(1), 1–17.

Adam, J., Green, T. H., & Sie, S. H. (1993). Proton microprobe determined partitioning of Rb, Sr, Ba, Y, Zr, Nb and Ta between experimentally produced amphiboles and silicate melts with variable F content. *Chemical Geology*, *109*(1-4), 29–49.

Aiuppa, A., Baker, D. R., & Webster, J. D. (2009). Halogens in volcanic systems. *Chemical Geology*, *263*(1-4), 1–18.

Albert, H., Costa, F., & Martí, J. (2015). Timing of magmatic processes and unrest associated with mafic historical monogenetic eruptions in Tenerife Island. *Journal of Petrology*, *56*(10), 1945–1966.

Andújar, J. & Scaillet, B. (2012). Experimental constraints on parameters controlling the difference in the eruptive dynamics of phonolitic magmas: the case of Tenerife (Canary Islands). *Journal of Petrology*, *53*(9), 1777–1806.

Anenburg, M. & Walters, J. B. (2024). Metasomatic ijolite, glimmerite, silicocarbonatite, and antiskarn formation: carbonatite and silicate phase equilibria in the system Na_2O–CaO–K_2O–FeO–MgO–Al_2O_3–SiO_2–H_2O–O_2–CO_2. *Contributions to Mineralogy and Petrology*, *179*(5), 40.

Aseri, A. A., Linnen, R. L., Che, X. D., Thibault, Y., & Holtz, F. (2015). Effects of fluorine on the solubilities of Nb, Ta, Zr and Hf minerals in highly fluxed water-saturated haplogranitic melts. *Ore Geology Reviews*, *64*, 736–746.

Asimow, P. D., Dixon, J. E., & Langmuir, C. H. (2004). A hydrous melting and fractionation model for mid-ocean ridge basalts: Application to the Mid-Atlantic Ridge near the Azores. *Geochemistry, Geophysics, Geosystems*, *5*(1).

Azadbakht, Z. & Lentz, D. R. (2020). High-resolution LA-ICP-MS trace-element mapping of magmatic biotite: A new approach for studying syn-to post-magmatic evolution. *The Canadian Mineralogist*, *58*(3), 293–311.

Beard, C. D. (2018). *Mineral-melt trace element partitioning in alkaline magmatic systems*. Ph.D. thesis, McGill University, Montreal, Canada.

Beard, C. D., Goodenough, K. M., Borst, A. M., Wall, F., Siegfried, P. R., Deady, E. A., Pohl, C., Hutchison, W., Finch, A. A., Walter, B. F., Elliott, H. A., & Brauch, K. (2023). Alkaline-silicate REE-HFSE systems. *Economic Geology*, *118*(1), 177–208.

Beard, C. D., van Hinsberg, V. J., Stix, J., & Wilke, M. (2019). Clinopyroxene/melt trace element partitioning in sodic alkaline magmas. *Journal of Petrology*, *60*(9), 1797–1823.

Beard, C. D., van Hinsberg, V. J., Stix, J., & Wilke, M. (2020). The effect of fluorine on clinopyroxene/melt trace-element partitioning. *Contributions to Mineralogy and Petrology*, *175*(5), 44.

Bédard, J. H. (2001). Parental magmas of the nain plutonic suite anorthosites and mafic cumulates: a trace element modelling approach. *Contributions to Mineralogy and Petrology*, *141*(6), 747–771.

Bédard, J. H. (2014). Parameterizations of calcic clinopyroxene — Melt trace element partition coefficients. *Geochemistry, Geophysics, Geosystems*, *15*(2), 303–336.

Bédard, J. H. (2023). Trace element partitioning coefficients between terrestrial silicate melts and plagioclase feldspar: Improved and simplified parameters. *Geochimica et Cosmochimica Acta*, *350*, 69–86.

Behrens, H. (2020). Water speciation in oxide glasses and melts. *Chemical Geology*, *558*, 119850.

Berndt, J., Liebske, C., Holtz, F., Freise, M., Nowak, M., Ziegenbein, D., Hurkuck, W., & Koepke, J. (2002). A combined rapid-quench and H_2-membrane setup for internally heated pressure vessels: Description and application for water solubility in basaltic melts. *American Mineralogist*, *87*(11-12), 1717–1726.

Blundy, J. & Wood, B. (1994). Prediction of crystal–melt partition coefficients from elastic moduli. *Nature*, *372*(6505), 452–454.

Blundy, J. D., Robinson, J. A. C., & Wood, B. J. (1998). Heavy REE are compatible in clinopyroxene on the spinel lherzolite solidus. *Earth and Planetary Science Letters*, *160*(3–4), 493–504.

Botcharnikov, R. E., Behrens, H., & Holtz, F. (2006). Solubility and speciation of C–O–H fluids in andesitic melt at T=1100–1300 °C and P=200 and 500MPa. *Chemical Geology*, *229*(1), 125–143.

Breasley, C. M., Groat, L. A., Martins, T., Linnen, R. L., Larson, K. P., & Henry, R. E. (2024). Mineralogy and petrology of the petalite-subtype Prof pegmatite, Revelstoke, British Columbia, Canada. *Mineralogical Magazine*, *88*(6), 698–720.

Breiter, K., Galiová, M. V., Korbelová, Z., & Hložková, M. (2023). Can lithium contents in mica be correctly calculated? Tischendorfs proposal (Mineralogical Magazine 61/1997) 25 years after. *Mineralogical Magazine*, *87*(6), 878–886.

Brice, J. C. (1975). Some thermodynamic aspects of the growth of strained crystals. *Journal of Crystal Growth*, *28*(2), 249–253.

Brigatti, M. F. & Guggenheim, S. (2002). Mica crystal chemistry and the influence of pressure, temperature, and solid solution on atomistic models. *Reviews in Mineralogy and Geochemistry*, *46*(1), 1–97.

Černý, P., Masau, M., Goad, B. E., & Ferreira, K. (2005). The Greer Lake leucogranite, Manitoba, and the origin of lepidolite-subtype granitic pegmatites. *Lithos*, *80*(1-4 SPEC. ISS.), 305–321.

Cherniak, D. J. & Dimanov, A. (2010). Diffusion in pyroxene, mica and amphibole. *Reviews in Mineralogy and Geochemistry*, *72*(1), 641–690.

Deer, W. A., Howie, R. A., & Zussman, J. (1992). *An introduction to the rock-forming minerals*. New York: Longman Group Ltd.

Dingwell, D. B., Scarfe, C. M., & Cronin, D. J. (1985). The effect of fluorine on viscosities in the system Na_2O–Al_2O_3–SiO_2: implications for phonolites, trachytes and rhyolites. *American Mineralogist*, *70*, 80–87.

Dolejš, D. & Baker, D. R. (2006). Fluorite solubility in hydrous haplogranitic melts at 100 MPa. *Chemical Geology*, *225*(1-2), 40–60.

Dolejš, D. & Baker, D. R. (2007). Liquidus equilibria in the system K_2O-Na_2O-Al_2O_3-SiO_2-F_2O_{-1}-H_2O to 100 MPa: II. Differentiation paths of fluorosilicic magmas in hydrous systems. *Journal of Petrology*, *48*(4), 807–828.

Ellis, B. S., Neukampf, J., Bachmann, O., Harris, C., Forni, F., Magna, T., Laurent, O., & Ulmer, P. (2022). Biotite as a recorder of an exsolved Li-rich volatile phase in upper-crustal silicic magma reservoirs. *Geology*, *50*(4), 481–485.

Evensen, J. M. & London, D. (2002). Experimental silicate mineral/melt partition coefficients for beryllium and the crustal be cycle from migmatite to pegmatite. *Geochimica et Cosmochimica Acta*, *66*(12), 2239–2265.

Ezad, I. S. & Foley, S. F. (2022). Experimental partitioning of fluorine and barium in lamproites. *American Mineralogist*, *107*(11), 2008–2019.

Fabbrizio, A. & Carroll, M. R. (2008). Experimental constraints on the differentiation process and pre-eruptive conditions in the magmatic system of Phlegraean Fields (Naples, Italy).

Farges, F. F. (1996). Does Zr-F “complexation” occur in magmas? *Chemical Geology*, *127*(4), 253–268.

Finch, A. A., Parsons, I., & Mingard, S. C. (1995). Biotites as indicators of fluorine fugacities in late-stage magmatic fluids: The Gardar Province of South Greenland. *Journal of Petrology*, *36*(6), 1701–1728.

Finch, E. & Tomkins, A. (2017). Fluorine and chlorine behaviour during progressive dehydration melting: Consequences for granite geochemistry and metallogeny. *Journal of Metamorphic Geology*, *35*(7), 739–757.

Fitzpayne, A., Giuliani, A., Phillips, D., Hergt, J., Woodhead, J. D., Farquhar, J., Fiorentini, M. L., Drysdale, R. N., & Wu, N. (2018). Kimberlite-related metasomatism recorded in marid and pic mantle xenoliths. *Mineralogy and Petrology*, *112*(1), 71–84.

Fleet, M. E. (2003). *Rock-Forming Minerals, vol. 3A Sheet silicates: micas*. London: The Geological Society, 2nd ed.

Förster, H. J., Tischendorf, G., Trumbull, R. B., & Gottesmann, B. (1999). Late-collisional granites in the Variscan Erzgebirge, Germany. *Journal of Petrology*, *40*(11), 1613–1645.

Frost, B. R., Barnes, C. G., Collins, W. J., Arculus, R. J., Ellis, D. J., & Frost, C. D. (2001). A geochemical classification for granitic rocks. *Journal of Petrology*, *42*(11), 2033–2048.

Gardiner, N. J., Palin, R. M., Koopmans, L., Mangler, M. F., & Robb, L. J. (2024). On tin and lithium granite systems: a crustal evolution perspective. *Earth-Science Reviews*, 104947.

Ghiorso, M. S., Hirschmann, M. M., Reiners, P. W., & Kress III, V. C. (2002). The pMELTS: A revision of MELTS for improved calculation of phase relations and major element partitioning related to partial melting of the mantle to 3 GPa. *Geochemistry, Geophysics, Geosystems*, *3*(5), 1–35.

Ghiorso, M. S. & Sack, R. O. (1995). Chemical mass transfer in magmatic processes IV. A revised and internally consistent thermodynamic model for the interpolation and extrapolation of liquid-solid equilibria in magmatic systems at elevated temperatures and pressures. *Contributions to Mineralogy and Petrology*, *119*(2-3), 197–212.

Gianfagna, A., Scordari, F., Mazziotti-Tagliani, S., Ventruti, G., & Ottolini, L. (2007). Fluorophlogopite from Biancavilla (Mt. Etna, Sicily, Italy): Crystal structure and crystal chemistry of a new F-dominant analog of phlogopite. *American Mineralogist*, *92*(10), 1601–1609.

Giebel, R. J., Marks, M. A., Gauert, C. D., & Markl, G. (2019). A model for the formation of carbonatite-phoscorite assemblages based on the compositional variations of mica and apatite from the Palabora Carbonatite Complex, South Africa. *Lithos*, *324-325*, 89–104.

Giehl, C., Marks, M. A. W., & Nowak, M. (2014). An experimental study on the influence of fluorine and chlorine on phase relations in peralkaline phonolitic melts. *Contributions to Mineralogy and Petrology*, *167*(3), 1–21.

Giordano, D., Nichols, A., & Dingwell, D. (2005). Glass transition temperatures of natural hydrous melts: a relationship with shear viscosity and implications for the welding process. *Journal of Volcanology and Geothermal Research*, *142*(1-2), 105–118.

Goodenough, K., Shaw, R., Borst, A., Nex, P., Kinnaird, J., Van Lichtervelde, M., Essaifi, A., Koopmans, L., & Deady, E. (2025). Lithium pegmatites in Africa: A review. *Economic Geology*, *120*(3), 513–539.

Govindaraju, K. (1994). 1994 compilation of working values and sample description for 383 geostandards. *Geostandards Newsletter*, *18*(S1), 1–158.

Gray, W., Glazner, A. F., Coleman, D. S., & Bartley, J. M. (2008). Long-term geochemical variability of the Late Cretaceous Tuolumne intrusive suite, central Sierra Nevada, California. *Geological Society, London, Special Publications*, *304*, 183–201.

Green, E. C., Holland, T. J., Powell, R., Weller, O. M., & Riel, N. (2025). Corrigendum to: Melting of peridotites through to granites: a simple thermodynamic model in the system KNCFMASHTOCr, and, a thermodynamic model for the subsolidus evolution and melting of peridotite. *Journal of Petrology*, *66*(1), egae079.

Green, T. H., Blundy, J. D., Adam, J., & Yaxley, G. M. (2000). SIMS determination of trace element partition coefficients between garnet, clinopyroxene and hydrous basaltic liquids at 2–7.5 GPa and 1080–1200ºC. *Lithos*, *53*(3–4), 165–187.

Grégoire, M., Bell, D., & Le Roex, A. (2002). Trace element geochemistry of phlogopite-rich mafic mantle xenoliths: their classification and their relationship to phlogopite-bearing peridotites and kimberlites revisited. *Contributions to Mineralogy and Petrology*, *142*(5), 603–625.

Gualda, G. A. R., Ghiorso, M. S., Lemons, R. V., & Carley, T. L. (2012). Rhyolite-MELTS: a modified calibration of MELTS optimized for silica-rich, fluid-bearing magmatic systems. *Journal of Petrology*, *53*(5), 875–890.

Guo, J. & Green, T. H. (1990). Experimental study of barium partitioning between phlogopite and silicate liquid at upper-mantle pressure and temperature. *Lithos*, *24*(2), 83–95.

Hammouda, T. Y. & Cherniak, D. J. (2000). Diffusion of Sr in fluorphlogopite determined by Rutherford backscattering spectrometry. *Earth and Planetary Science Letters*, *178*, 339–349.

Heinonen, J. S., Bohrson, W. A., Spera, F. J., Brown, G. A., Scruggs, M. A., & Adams, J. V. (2020). Diagnosing open-system magmatic processes using the Magma Chamber Simulator (MCS): part II—trace elements and isotopes. *Contributions to Mineralogy and Petrology*, *175*(11), 1–21.

Henry, D. J., Guidotti, C. V., & Thomson, J. A. (2005). The Ti-saturation surface for low-to-medium pressure metapelitic biotites: Implications for geothermometry and Ti-substitution mechanisms. *American Mineralogist*, *90*(2-3), 316–328.

Hirschmann, M. M., Ghiorso, M. S., Davis, F. A., Gordon, S. M., Mukherjee, S., Grove, T. L., Krawczynski, M., Medard, E., & Till, C. B. (2008). Library of Experimental Phase Relations (LEPR): A database and web portal for experimental magmatic phase equilibria data. *Geochemistry, Geophysics, Geosystems*, *9*(3), 1–15.

Holland, T. J. B., Green, E. C. R., & Powell, R. (2018). Melting of peridotites through to granites: a simple thermodynamic model in the system KNCFMASHTOCr. *Journal of Petrology*, *59*(5), 881–900.

Holland, T. J. B. & Powell, R. (2011). An improved and extended internally consistent thermodynamic dataset for phases of petrological interest, involving a new equation of state for solids. *Journal of Metamorphic Geology*, *29*(3), 333–383.

Horányi, B., Gion, A. M., Gaillard, F., Gloaguen, É., Plunder, A., Melleton, J., Moradell-Casellas, A., Garde, J., Erdmann, S., & Di Carlo, I. (2025). Experimental constraints on the sources of lithium-rich granites and pegmatites. *Communications Earth & Environment*, *6*(1), 966.

Humphreys, M. C. S., Smith, V. C., Coumans, J. P., Riker, J. M., Stock, M. J., de Hoog, J. C. M., & Brooker, R. A. (2021). Rapid pre-eruptive mush reorganisation and atmospheric volatile emissions from the 12.9 ka Laacher See eruption, determined using apatite. *Earth and Planetary Science Letters*, *576*, 117198.

Icenhower, J. & London, D. (1995). An experimental study of element partitioning among biotite, muscovite, and coexisting peraluminous silicic melt at 200 MPa (H_2O). *American Mineralogist*, *80*(11-12), 1229–1251.

Icenhower, J. P. & London, D. (1997). Partitioning of fluorine and chlorine between biotite and granitic melt: experimental calibration at 200 MPa H_2O. *Contributions to Mineralogy and Petrology*, *127*(1-2), 17–29.

Jochum, K. P., Nohl, U., Herwig, K., Lammel, E., Stoll, B., & Hofmann, A. W. (2005). GeoReM: a new geochemical database for reference materials and isotopic standards. *Geostandards and Geoanalytical Research*, *29*(3), 333–338.

Jochum, K. P., Weis, U., Schwager, B., Stoll, B., Wilson, S. A., Haug, G. H., Andreae, M. O., & Enzweiler, J. (2016). Reference values following ISO guidelines for frequently requested rock reference materials. *Geostandards and Geoanalytical Research*, *40*(3), 333–350.

Jochum, K. P., Weis, U., Stoll, B., Kuzmin, D., Yang, Q., Raczek, I., Jacob, D. E., Stracke, A., Birbaum, K., & Frick, D. A. (2011). Determination of reference values for NIST SRM 610–617 glasses following ISO guidelines. *Geostandards and geoanalytical research*, *35*(4), 397–429.

Jugo, P. J., Wilke, M., & Botcharnikov, R. E. (2010). Sulfur K-edge XANES analysis of natural and synthetic basaltic glasses: Implications for S speciation and S content as function of oxygen fugacity. *Geochimica et Cosmochimica Acta*, *74*(20), 5926–5938.

Koopmans, L., Martins, T., Linnen, R., Gardiner, N. J., Breasley, C. M., Palin, R. M., Groat, L. A., Silva, D., & Robb, L. J. (2024). The formation of lithium-rich pegmatites through multi-stage melting. *Geology*, *52*(1), 7–11.

Kunz, B. E., Warren, C. J., Jenner, F. E., Harris, N. B., & Argles, T. W. (2022). Critical metal enrichment in crustal melts: The role of metamorphic mica. *Geology*, *50*(11), 1219–1223.

Lanin, E. S., Sone, H., Yu, Z., Liu, Q., & Wang, B. (2021). Comparison of biotite elastic properties recovered by spherical nanoindentations and atomistic simulations — influence of nano-scale defects in phyllosilicates. *Journal of Geophysical Research: Solid Earth*, *126*(8), e2021JB021902.

LaTourrette, T., Hervig, R. L., & Holloway, J. R. (1995). Trace element partitioning between amphibole, phologopite, and basanite melt. *Earth and Planetary Science Letters*, *l35*(1), 13–30.

Le Maitre, R. W., Streckeisen, A., Zanettin, B., Le Bas, M. J., Bonin, B., & Bateman, P. (2005). *Igneous rocks: a classification and glossary of terms: recommendations of the International Union of Geological Sciences Subcommission on the Systematics of Igneous Rocks*. Cambridge University Press.

Li, W. & Costa, F. (2020). A thermodynamic model for F-Cl-OH partitioning between silicate melts and apatite including non-ideal mixing with application to constraining melt volatile budgets. *Geochimica et Cosmochimica Acta*, *269*, 203–222.

Li, X. & Zhang, C. (2022). Machine learning thermobarometry for biotite-bearing magmas. *Journal of Geophysical Research: Solid Earth*, *127*(9), e2022JB024137.

Li, X., Zhang, C., Behrens, H., & Holtz, F. (2020). Calculating biotite formula from electron microprobe analysis data using a machine learning method based on principal components regression. *Lithos*, *356-357*, 105371.

Linnen, R. L., Van Lichtervelde, M., & Černý, P. (2012). Granitic pegmatites as sources of strategic metals. *Elements*, *8*(4), 275–280.

Loiselle, M. & Wones, D. R. (1979). Characteristics and origin of anorogenic granites. *Geol. Soc. Am.*, *11*, 468.

London, D. (1987). Internal differentiation of rare-element pegmatites: Effects of boron, phosphorus, and fluorine. *Geochimica et Cosmochimica Acta*, *51*(3), 403–420.

London, D. (1997). Estimating abundances of volatile and other mobile components in evolved silicic melts through mineral–melt equilibria. *Journal of Petrology*, *38*(12), 1691–1706.

London, D. (2018). Ore-forming processes within granitic pegmatites. *Ore Geology Reviews*, *101*, 349–383.

Lukkari, S. & Holtz, F. (2007). Phase relations of a F-enriched peraluminous granite: an experimental study of the Kymi topaz granite stock, southern Finland. *Contributions to Mineralogy and Petrology*, *153*(3), 273–288.

Marks, M. A. & Markl, G. (2017). A global review on agpaitic rocks.

Martins, T., Roda-Robles, E., Lima, A., & de Parseval, P. (2012). Geochemistry and evolution of micas in the Barroso–Alvão pegmatite field, Northern Portugal. *The Canadian Mineralogist*, *50*(4), 1117–1129.

Masotta, M., Pontesilli, A., Mollo, S., Armienti, P., Ubide, T., Nazzari, M., & Scarlato, P. (2020). The role of undercooling during clinopyroxene growth in trachybasaltic magmas: Insights on magma decompression and cooling at Mt. Etna volcano. *Geochimica et Cosmochimica Acta*, *268*, 258–276.

McCubbin, F. M., Vander Kaaden, K. E., Tartèse, R., Boyce, J. W., Mikhail, S., Whitson, E. S., Bell, A. S., Anand, M., Franchi, I. A., & Wang, J. (2015). Experimental investigation of F, Cl, and OH partitioning between apatite and Fe-rich basaltic melt at 1.0–1.2 GPa and 950–1000 C. *American Mineralogist*, *100*(8-9), 1790–1802.

Mills, K. C. (1993). The influence of structure on the physico-chemical properties of slags. *ISIJ international*, *33*(1), 148–155.

Möller, V. & Williams-Jones, A. E. (2016). Petrogenesis of the Nechalacho layered suite, Canada: Magmatic evolution of a REE-Nb-rich nepheline syenite intrusion. *Journal of Petrology*, *57*(2), 229–276.

Mollo, S., Blundy, J., Scarlato, P., Vetere, F., Holtz, F., Bachmann, O., & Gaeta, M. (2020). A review of the lattice strain and electrostatic effects on trace element partitioning between clinopyroxene and melt: Applications to magmatic systems saturated with Tschermak-rich clinopyroxenes. *Earth-Science Reviews*, *210*, 103351.

Morgan vi, G. B. & London, D. (2005). Effect of current density on the electron microprobe analysis of alkali aluminosilicate glasses. *American Mineralogist*, *90*(7), 1131–1138.

Morris, M. C., Weller, O. M., Soderman, C. R., Edmonds, M., Beard, C. D., & Yeomans, C. M. (2026, accepted). The role of fluorine in the petrogenesis of Li-granites. *Nature Communications Earth and Environment*.

Munoz, J. L. (1984). F-OH and Cl-OH exchange in micas with applications to hydrothermal ore deposits. *Reviews in Mineralogy and Geochemistry*, *13*(1), 469–493.

Nathwani, C. L., Large, S. J., Brugge, E. R., Wilkinson, J. J., Buret, Y., & EIMF (2023). Apatite evidence for a fluid-saturated, crystal-rich magma reservoir forming the Quellaveco porphyry copper deposit (Southern Peru). *Contributions to Mineralogy and Petrology*, *178*(8), 49.

Nesbitt, H. W. & Young, G. M. (1984). Prediction of some weathering trends of plutonic and volcanic rocks based on thermodynamic and kinetic considerations. *Geochimica et Cosmochimica Acta*, *48*(7), 1523–1534.

Neukampf, J., Ellis, B. S., Magna, T., Laurent, O., & Marrocchi, Y. (2023). Partitioning and isotopic fractionation of li between mineral phases and alkaline to calc-alkaline melts of explosive and effusive eruptions. *Chemical Geology*, *636*, 121628.

O'Brien, H., Heilimo, E., & Heino, P. (2015). The Archean Siilinjärvi carbonatite complex. In W. D. Maier, R. Lahtinen, & H. O'Brien (Eds.), *Mineral Deposits of Finland*, Amsterdam: Elsevier Inc. 327–343.

Onuma, N., Higuchi, H., Wakita, H., & Nagasawa, H. (1968). Trace element partition between two pyroxenes and the host lava. *Earth and Planetary Science Letters*, *5*, 47–51.

Patiño Douce, A. E. (1993). Titanium substitution in biotite: an empirical model with applications to thermometry, O_2 and H_2O barometries, and consequences for biotite stability. *Chemical Geology*, *108*(1-4), 133–162.

Patiño Douce, A. E., Johnston, A. D., & Rice, J. M. (1993). Octahedral excess mixing properties in biotite: a working model with applications to geobarometry and geothermometry. *American Mineralogist*, *78*(1-2), 113–131.

Paton, C., Hellstrom, J., Paul, B., Woodhead, J., & Hergt, J. (2011). Iolite: Freeware for the visualisation and processing of mass spectrometric data. *Journal of Analytical Atomic Spectrometry*, *26*(12), 2508–2518.

Peterson, J. W., Chacko, T., & Kuehner, S. M. (1991). The effects of fluorine on the vapor-absent melting of phlogopite + quartz; implications for deep-crustal processes. *American Mineralogist*, *76*(3-4), 470–476.

Pichavant, M., Villaros, A., Deveaud, S., Scaillet, B., & Lahlafi, M. (2016). The influence of redox state on mica crystallization in leucogranitic and pegmatitic liquids. *The Canadian Mineralogist*, *54*(3), 559–581.

Ponader, C. W. & Brown Jr., G. E. (1989). Rare earth elements in silicate glass/melt systems: II. Interactions of La, Gd, and Yb with halogens. *Geochimica et Cosmochimica Acta*, *53*(11), 2905–2914.

Rayner, J. H. (1974). The crystal structure of phlogopite by neutron diffraction. *Mineralogical Magazine*, *39*(308), 850–856.

Rieder, M., Cavazzini, G., D'yakonov, Y. S., Frank-Kamenetskii, V. A., Gottardi, G., Guggenheim, S., Koval, P. W., Mueller, G., Neiva, A. M. R., Radoslovich, E. W., Robert, J.-L., Sassi, F. P., Takeda, H., Weiss, Z., & Wones, D. R. (1998). Nomenclature of the micas. *The Canadian Mineralogist*, *36*, 41–48.

Riel, N., Kaus, B. J. P., Green, E. C. R., & Berlie, N. (2022). MAGEMin, an efficient Gibbs energy minimizer: application to igneous systems. *Geochemistry, Geophysics, Geosystems*, *23*(7), e2022GC010427.

Righter, K. & Carmichael, I. S. E. (1996). Phase equilibria of phlogopite lamprophyres from western Mexico: biotite-liquid equilibria and P-T estimates for biotite-bearing igneous rocks. *Contributions to Mineralogy and Petrology*, *123*(1), 1–21.

Riker, J., Humphreys, M. C., Brooker, R. A., De Hoog, J. C., & Eim, F. (2018). First measurements of OH-C exchange and temperature-dependent partitioning of OH and halogens in the system apatite-silicate melt. *American Mineralogist*, *103*(2), 260–270.

Rosenberg, P. E. & Foit, F. F. (1977). Fe^{2+} –F avoidance in silicates. *Geochimica et Cosmochimica Acta*, *41*(2), 345–346.

Rubatto, D. & Hermann, J. (2007). Experimental zircon/melt and zircon/garnet trace element partitioning and implications for the geochronology of crustal rocks. *Chemical Geology*, *241*(1–2), 38–61.

Schmidt, K. H., Bottazzi, P., Vannucci, R., & Mengel, K. (1999). Trace element partitioning between phlogopite, clinopyroxene and leucite lamproite melt. *Earth and Planetary Science Letters*, *168*(3-4), 287–299.

Shannon, R. (1976). Revised effective ionic radii and systematic studies of interatomic distances in halides and chalcogenides. *Acta Crystallographica Section A*, *32*(5), 751–767.

Siegel, K., Vasyukova, O. V., & Williams-Jones, A. E. (2018). Magmatic evolution and controls on rare metal-enrichment of the Strange Lake A-type peralkaline granitic pluton, Québec-Labrador. *Lithos*, *308-309*, 34–52.

Sievwright, R. H., Wilkinson, J. J., O'Neill, H. S. C., & Berry, A. J. (2017). Thermodynamic controls on element partitioning between titanomagnetite and andesitic–dacitic silicate melts. *Contributions to Mineralogy and Petrology*, *172*(8), 62.

Simons, B., Shail, R. K., & Andersen, J. C. (2016). The petrogenesis of the Early Permian Variscan granites of the Cornubian Batholith: Lower plate post-collisional peraluminous magmatism in the Rhenohercynian Zone of SW England. *Lithos*, *260*, 76–94.

Sliwinski, J. T., Ellis, B. S., Dávila-Harris, P., Wolff, J. A., Olin, P. H., & Bachmann, O. (2017). The use of biotite trace element compositions for fingerprinting magma batches at Las Cañadas volcano, Tenerife. *Bulletin of Volcanology*, *79*(1), 1.

Smith, D. (1995). USGS certificate of analysis, rhyolite, Glass Mountain, RGM-1.

Soderman, C. R., Weller, O. M., Beard, C. D., Riel, N., Green, E. C. R., & Holland, T. J. B. (2025). A mid-crustal tipping point between silica-undersaturated and silica-oversaturated magmas. *Nature Geoscience*, *18*, 555–562.

Speer, J. A. (1984). Micas in igneous rocks. *Reviews in Mineralogy and Geochemistry*, *13*(1), 299–356.

Sun, C., Graff, M., & Liang, Y. (2017). Trace element partitioning between plagioclase and silicate melt: The importance of temperature and plagioclase composition, with implications for terrestrial and lunar magmatism. *Geochimica et Cosmochimica Acta*, *206*, 273–295.

Tappe, S., Beard, C. D., Borst, A. M., Humphreys-Williams, E. R., Walter, B. F., & Yaxley, G. M. (2025). Kimberlite, carbonatite and alkaline magmatic systems: definitions, origins, and strategic mineral resources. In *Encyclopedia of Volcanoes, Third Edition*, Elsevier, chap. 8.2.2. 26.

Teng, F.-Z., Rudnick, R. L., McDonough, W. F., & Wu, F.-Y. (2009). Lithium isotopic systematics of A-type granites and their mafic enclaves: Further constraints on the Li isotopic composition of the continental crust. *Chemical Geology*, *262*(3), 370–379.

Ubide, T., Mollo, S., Zhao, J.-x., Nazzari, M., & Scarlato, P. (2019). Sector-zoned clinopyroxene as a recorder of magma history, eruption triggers, and ascent rates. *Geochimica et Cosmochimica Acta*.

van Hinsberg, V. J., Migdisov, A. A., & Williams-Jones, A. E. (2010). Reading the mineral record of fluid composition from element partitioning. *Geology*, *38*(9), 847–850.

Vasyukova, O. & Williams-Jones, A. E. (2016). The evolution of immiscible silicate and fluoride melts: Implications for REE ore-genesis. *Geochimica et Cosmochimica Acta*, *172*, 205–224.

Vasyukova, O. V. & Williams-Jones, A. E. (2022). Constraints on the genesis of cobalt deposits: Part II. Applications to natural systems. *Economic Geology*, *117*(3), 529–544.

Weller, O. M., Holland, T. J. B., Soderman, C. R., Green, E. C. R., Powell, R., Beard, C. D., & Riel, N. (2024). New thermodynamic models for anhydrous alkaline-silicate magmatic systems. *Journal of Petrology*, *65*(10), egae098.

Wood, B. J. & Blundy, J. D. (1997). A predictive model for rare earth element partitioning between clinopyroxene and anhydrous silicate melt. *Contributions to Mineralogy and Petrology*, *129*(2-3), 166–181.

Wood, B. J. & Blundy, J. D. (2003). Trace element partitioning under crustal and uppermost mantle conditions: The influences of ionic radius, cation charge, pressure, and temperature. In R. W. Carlson (Ed.), *The Mantle and Core: Treatise on Geochemistry*, Elsevier, vol. 2, chap. 2.09. 395–424.

Wood, B. J. & Blundy, J. D. (2014). Trace element partitioning: The influences of ionic radius, cation charge, pressure, and temperature. In R. W. Carlson (Ed.), *The Mantle and Core: Treatise on Geochemistry: Second Edition*, Elsevier, chap. 3.11. 421–445.

Wu, M., Samson, I. M., Borst, A. M., Diao, X., Beard, C. D., Zheng, X., Fan, M., Hou, Z., & Qiu, K. (2025). Quartz-petalite intergrowths in the Yichun pegmatite: Formation from late-stage Li-rich melts and implications for Li mineralization in rare-metal granites. *American Mineralogist*.

Wyllie, P. J. & Tuttle, O. F. (1961). Experimental investigation of silicate systems containing two volatile components; Part 2, The effects of NH_3 and HF, in addition to H_2O on the melting temperatures of albite and granite. *American Journal of Science*, *259*(2), 128–143.

Xue, S., Dasgupta, R., Ling, M.-X., Sun, W., & Lee, C.-T. A. (2024). The effect of fluorine on mineral-carbonatitic melt partitioning of trace elements–implications for critical mineral deposits. *Geochimica et Cosmochimica Acta*, *379*, 53–75.

Yakymchuk, C., Clark, C., & White, R. W. (2017). Phase relations, reaction sequences and petrochronology. *Reviews in Mineralogy and Geochemistry*, *83*(1), 13–53.

Yang, L. & van Hinsberg, V. J. (2019). Liquid immiscibility in the CaF 2 -granite system and trace element partitioning between the immiscible liquids. *Chemical Geology*, *511*(September 2018), 28–41.

Yang, L., van Hinsberg, V. J., & Samson, I. M. (2018). A new method to deconvolute binary mixture in LA-ICP-MS analyses to quantify the composition of phases smaller than the laser spot size. *Journal of Analytical Atomic Spectrometry*, *33*(9), 1518–1528.

Yang, Z.-Y., Wu, M.-Q., Li, S.-S., Yu, H.-C., Diao, X., Gao, Y.-X., Ma, J.-D., Zhi, C.-L., Shang, Z., Xi, J.-K., Huang, Y.-Q., & Qiu, K.-F. (2025). The origin of glimmerite and its significance to rare earth element mineralization: Insights from the Longbaoshan deposit in North China Craton. *Ore Geology Reviews*, *184*, 106698.

Zhang, C., Li, X., Behrens, H., & Holtz, F. (2022). Partitioning of OH-F-Cl between biotite and silicate melt: Experiments and an empirical model. *Geochimica et Cosmochimica Acta*, *317*, 155–179.

Tables

Table 1 Major-element oxide composition of starting materials for the internally heated pressure vessel experiments. The totals are calculated with all iron as FeO. The standard deviation (σ) and relative standard deviation (RSD) are given for EPMA measurements of glass from a superliquidus experiment.

Dry starting glass composition calculated from masses of reagents added [wt%]

Composition	SiO_2	TiO_2	Al_2O_3	FeO_T	MgO	CaO	Na_2O	K_2O	Total	(Na+K)/Al
M3	52.67	2.27	18.13	7.86	2.75	5.40	7.19	3.73	100.00	0.875
M5	60.04	0.66	19.13	3.69	0.42	0.89	9.76	5.41	100.00	1.145
H5	58.38	0.65	18.60	3.59	0.41	0.86	11.31	6.20	100.00	1.362
Water saturated glass compositions from a superliquidus experiment (EPMA) [wt%]										
H5 (fluorine free)	55.5	0.61	16.2	2.6.	0.42	0.91	10.8	5.7	92.8	1.48
σ (n = 13)	0.3	0.06	0.2	0.1	0.04	0.05	0.2	0.2	0.4	0.03
RSD	0.59%	9.33%	1.36%	4.41%	10.44%	5.40%	1.90%	2.69%	0.45%	1.87%

Table 2 Major-element oxide composition (in wt%) of biotite from the experiments and Canary Islands rocks. The standard deviation (σ) and relative standard deviation (RSD) are given for the EPMA data.

	SiO_2	TiO_2	Al_2O_3	FeO_T	MnO	MgO	CaO	Na_2O	K_2O	F	Cl	Total
16-07	36.6	6.9	12.7	15.5	0.43	13.7	0.01	0.97	8.51	0.7	0.02	95.9
σ (n = 31)	0.4	0.2	0.4	0.5	0.03	0.3	0.02	0.04	0.09	0.2	0.01	0.7
RSD	1.06%	2.72%	3.37%	2.88%	7.95%	2.31%	121.11%	3.62%	1.02%	25.70%	44.16%	0.68%
21-30	36.86	6.718	12.64	15.92	0.467	13.70	0.007	0.952	8.580	0.666	0.020	96.25
σ (n = 24)	0.41	0.39	0.19	1.06	0.06	0.81	0.01	0.05	0.09	0.19	0.01	0.96
RSD	1.11%	5.74%	1.48%	6.64%	13.13%	5.95%	157.95%	5.63%	1.09%	29.02%	31.71%	1.00%
17-12	36.91	7.606	13.05	13.57	0.278	14.71	0.003	1.128	8.274	0.675	0.023	94.71
σ (n = 12)	0.27	0.14	0.11	0.12	0.04	0.28	0.00	0.02	0.09	0.22	0.01	1.99
RSD	0.74%	1.90%	0.81%	0.89%	13.64%	1.91%	92.44%	1.91%	1.07%	33.18%	33.58%	2.11%
17-14	36.63	6.690	12.52	16.45	0.479	13.26	0.011	0.940	8.582	0.660	0.019	95.96
σ (n = 25)	0.46	0.12	0.23	0.20	0.01	0.16	0.02	0.03	0.14	0.15	0.01	0.83
RSD	1.25%	1.76%	1.81%	1.19%	3.01%	1.23%	169.33%	3.46%	1.60%	23.19%	33.74%	0.87%
M3_2	38.19	4.467	13.73	9.546	-	19.76	0.040	1.162	8.403	-	-	95.32
σ (n = 10)	0.97	0.17	0.62	0.87		0.54	0.03	0.06	0.13			1.99
RSD	2.55%	3.72%	4.49%	9.14%		2.76%	67.24%	5.33%	1.56%			2.09%
M3_0.6F	39.42	2.909	12.40	8.105	-	21.47	0.037	1.209	8.659	2.710	0.004	96.93
σ (n = 9)	0.97	0.19	0.33	0.34		0.55	0.02	0.05	0.09	0.51	0.00	1.49
RSD	2.46%	6.60%	2.67%	4.21%		2.55%	46.74%	4.02%	0.99%	18.95%		1.53%
M5_2.5F Top	44.64	2.460	8.593	10.10	-	17.59	0.002	0.663	9.748	5.268	0.024	99.12
σ (n = 4)	0.56	0.21	0.38	0.62		0.22	0.00	0.03	0.20	0.30	0.02	0.29
RSD	1.25%	8.44%	4.45%	6.15%		1.24%		4.67%	2.00%	5.78%		0.29%

Table 3 Major-element oxide composition (in wt%) of quenched melts from the experiments and Canary Islands rocks.

	SiO_2	TiO_2	Al_2O_3	FeO_T	MnO	MgO	CaO	Na_2O	K_2O	F	Cl	Total
21-30 Pico Viejo	60.40	0.642	19.85	3.481	0.198	0.344	0.754	9.161	5.570	0.132	0.408	100.93
16-07 LMB	60.38	0.635	19.96	3.284	0.138	0.387	0.758	9.000	5.410	0.084	0.376	100.41
17-14 MBII	59.08	0.663	19.68	3.620	0.222	0.317	0.765	9.760	5.450	0.173	0.395	100.12
17-12 M. Samara	55.10	1.733	18.30	6.494	0.229	1.837	4.098	7.257	4.087	0.123	0.193	99.45
M3_2 (800°C)	57.29	0.265	19.14	1.217	-	0.126	0.954	7.319	4.097	-	-	90.41
M3_0.3F Gl[2:6, 8, 10]	58.95	0.283	19.51	1.283	-	0.142	0.984	7.834	4.036	0.110	0.005	93.16
M3_0.6F Gl[10 6]	58.63	0.278	19.60	1.365	-	0.121	0.824	8.170	4.215	0.123	0.009	93.35
M3_1.25F Gl[1:3]	57.47	0.248	19.64	1.660	-	0.138	0.720	8.520	4.233	0.157	0.010	92.82
M3_0.6F Gl[2 4 5]	58.15	0.129	19.76	1.530	-	0.125	1.228	7.990	4.123	0.956	0.011	94.01
M3_1.25F Gl[9:10]	56.10	0.166	19.36	1.835	-	0.167	1.359	8.710	4.195	1.535	0.017	93.45
M5_2 (700°C)	57.45	0.226	16.69	0.912	-	0.148	0.244	9.078	4.682	-	-	89.43
M5_0.3F Gl[1:4]	55.67	0.243	16.23	2.305	-	0.189	0.311	10.51	4.353	0.000	0.005	89.81
M5_0.6F Gl[6 8]	57.61	0.246	16.89	2.360	-	0.196	0.381	8.475	4.835	0.000	0.000	90.99
M5_0.3F Gl[7:9]	55.89	0.326	16.12	2.623	-	0.172	0.394	10.65	4.337	0.043	0.003	90.56
M5_1.25F Gl[1:4]	59.80	0.123	17.54	1.427	-	0.084	0.225	8.120	5.005	0.346	0.017	92.70
H5_3 (650°C)	54.91	0.618	16.06	2.843	-	0.346	0.837	8.880	5.301	-	-	89.81
H5_0.3F Gl[1:7]	55.72	0.238	16.16	2.426	-	0.187	0.309	10.66	4.331	0.000	0.004	90.03
H5_0.3F Gl[9:12]	55.57	0.390	16.03	2.845	-	0.161	0.421	10.58	4.365	0.127	0.003	90.48

Table 4 Biotite-melt partition coefficients from a selection of the Canary Islands pyroclastic rocks and internally heated pressure vessel experiments. EP indicates partition coefficients calculated from concentrations measured by EPMA. All others are from LA-ICP-MS. Analyses where either biotite or melt were below detection limit of our setup are denoted by '-'. Note that the experiments are Mn-free.

Name	21-30	σ	16-07	σ	17-12	σ	M3$_2$	σ	M3_0.6F	σ	M5_2.5F	σ	H5_1.25F$_2$	σ	H5$_3$	σ
	PicoViejo		LMB		M.Samara		Full capsule		Full capsule		Top		Top		Full capsule	
Li	0.90	0.70	0.72	0.59	0.23	0.14	0.48	0.04	0.82	0.07	19.80	0.34	23.82	5.23	3.05	1.21
Na	0.112	0.099	0.142	0.120	0.160	0.143	0.152	0.006	0.134	0.003	-	-	-	-	0.199	0.034
Mg	4	4	16	10	4	3	6	2	15	6	177	1	209	56	8	5
Si	0.67	0.58	0.62	0.58	0.67	0.63	0.68	0.04	0.66	0.03	0.64	0.03	0.72	0.19	0.79	0.10
K	1.49	1.32	1.78	1.59	1.87	1.67	1.50	0.25	1.78	0.20	1.73	0.03	2.30	0.39	1.43	0.35
Ca	0.008	0.007	0.026	0.015	0.006	0.004	0.098	0.013	0.032	0.012	0.209	0.107	-	-	-	-
Ti	9.6	8.4	10.5	10.2	10.6	9.9	3.8	1.0	4.1	0.9	3.6	0.1	4.7	0.9	3.3	1.2
Fe	3.0	2.6	4.4	3.7	2.7	2.3	2.9	0.8	2.6	0.6	6.3	0.1	4.4	0.7	2.4	0.7
Ga	1.0	0.9	1.8	1.4	5.9	4.0	1.9	0.4	2.6	0.3	3.5	0.3	2.4	0.7	1.3	0.2
Rb	1.75	1.56	2.27	1.99	1.75	1.53	1.74	0.31	2.15	0.28	2.09	0.05	2.84	0.51	1.96	0.52
Sr	0.17	0.09	0.16	0.08	0.33	0.15	0.20	0.02	0.19	0.02	-	-	0.00	-	0.10	0.06
Y	0.001	0.001	0.004	0.001	0.002	0.001	0.058	0.024	0.050	0.022	0.080	0.021	0.068	0.057	0.009	-
Zr	0.02	0.02	0.02	0.02	0.02	0.02	0.10	0.02	0.04	0.01	0.06	0.01	0.10	0.04	0.12	0.05
Nb	0.7	0.6	0.8	0.7	0.8	0.7	1.0	0.4	0.4	-	0.1	-	1.2	-	0.2	-
Cs	0.47	0.41	0.59	0.50	0.39	0.33	0.79	0.07	0.67	0.04	0.25	0.03	0.46	0.20	0.83	0.14
Ba	55.0	32.8	11.5	6.4	101.1	50.8	2.4	0.6	5.2	1.1	5.5	0.1	4.6	1.1	1.3	0.3
La	0.0001	-	0.0042	-	0.0004	-	-	-	-	-	-	-	-	-	-	-
Ce	-	-	0.0051	-	0.0003	-	-	-	-	-	-	-	-	-	-	-
Nd	-	-	0.0064	-	0.0003	-	-	-	-	-	-	-	-	-	-	-
Sm	-	-	0.0046	-	-	-	-	-	-	-	-	-	-	-	-	-
Eu	0.0139	0.0098	0.0364	-	0.0549	0.0234	-	-	-	-	-	-	-	-	-	-
Dy	-	0.0000	0.0030	-	-	-	-	-	-	-	-	-	-	-	-	-
Tm	0.0021	-	0.0028	-	-	-	-	-	-	-	-	-	-	-	-	-
Yb	0.0049	0.0036	0.0080	0.0039	0.0035	0.0005	-	-	-	-	-	-	-	-	-	-
Hf	0.02	0.01	0.02	0.02	0.02	0.02	0.16	0.04	0.04	0.01	0.03	0.02	0.10	0.07	0.06	0.04
Ta	0.4	0.4	0.4	0.4	0.5	0.4	1.0	0.4	0.9	0.3	1.0	0.9	-	-	0.6	0.3
Pb	0.02	0.01	0.03	0.02	0.03	0.03	0.08	0.01	0.08	0.01	0.15	0.04	-	-	0.83	0.37
Th	0.0001	-	0.0007	-	-	-	0.0051	-	0.0074	0.0051	0.1149	0.0320	0.0892	0.0706	0.0618	0.0292
U	0.001	0.001	0.002	0.001	0.001	0.001	0.015	0.007	0.007	0.005	-	-	-	-	0.074	0.041
Si_EP	0.61	0.01	0.61	0.02	0.71	0.04	0.66	0.03	0.64	0.03	0.70	0.03	0.72	0.07	0.71	0.04
Ti_EP	10.2	1.0	10.9	0.5	3.3	0.2	15.7	2.1	18.9	3.1	3.4	2.8	4.3	0.4	6.9	1.4
Al_EP	0.64	0.01	0.64	0.03	0.75	0.05	0.67	0.04	0.57	0.02	0.45	0.06	0.45	0.03	0.63	0.02
Fe_EP	4.5	0.4	4.7	0.2	1.7	0.2	8.0	1.3	5.3	0.3	6.1	3.7	4.9	0.4	6.0	0.9
Mn_EP	2.3	0.7	3.1	0.3	1.3	0.3										
Mg_EP	40	5	36	2	5.7	0.3	144	23	157	15	196	185	113	38	39	6
Ca_EP	0.009	-	0.019	-	-	-	0.039	0.027	0.026	0.013	0.024	-	0.024	-	0.017	0.013
Na_EP	0.11	0.02	0.11	0.01	0.17	0.02	0.15	0.01	0.13	0.01	0.07	0.01	0.06	0.00	0.05	0.00
K_EP	1.54	0.05	1.57	0.05	2.41	0.15	1.88	0.08	1.87	0.04	1.73	0.41	1.82	0.08	1.70	0.05
F_EP	4	2	8	2	4	2	-	-	2.3	0.7	2.0	0.5	2.3	0.5	-	-
Cl_EP	0.05	0.02	0.06	0.03	0.20	0.12	-	-	-	-	-	-	-	-	-	-

Model for LnKd F/OH (n = 229)

Parameter	Coefficient	σ
Intercept	-2.27	1.01
Bt Fe^{3+}/Fe$_{\mathrm{tot}}$	-1.35	0.26
$^{\mathrm{VI}}$MFe^{2+}	-0.565	0.209
$^{\mathrm{VI}}$MMg	0.535	0.158
$^{\mathrm{IV}}$TSi	1.54	0.27
$^{\mathrm{W}}$OH	-0.472	0.126
R^2; PRESS	0.640	0.632

Model for LnD_0^+, $^{\mathrm{XII}}$A-site (n = 43)

Parameter	Coefficient	σ
Intercept	-0.671	0.274
$^{\mathrm{XII}}$ANa	3.95	0.60
NBO/T melt	1.72	0.17
NK/Al melt	-0.850	0.095
10000/T [K]	0.179	0.028
	0.798	0.777

Model for r_0^+ [Å], $^{\mathrm{XII}}$A-site (n = 43, weighted)

Parameter	Coefficient	σ
Intercept	1.592	0.018
$^{\mathrm{VI}}$MFe^{2+}	0.0650	0.0172
$^{\mathrm{VI}}$MMg	0.0603	0.0078
$^{\mathrm{VI}}$MTi	-0.143	0.056
$^{\mathrm{W}}$F	-0.0214	0.0082
R^2; PRESS	0.823	0.805

Model for E^+ [GPa], $^{\mathrm{XII}}$A-site (n = 43)

Parameter	Coefficient	σ
Intercept	114	17
$^{\mathrm{XII}}$AK	-103	22
Bt Fe^{3+}/Fe$_{\mathrm{tot}}$	70.3	8.9
$^{\mathrm{VI}}$MFe^{3+}	-92.4	23.0
$^{\mathrm{VI}}$MTi	345	39
$^{\mathrm{W}}$O^{2-}	-110	15
	0.721	0.683

Model for LnD_{Li} (best; n = 43)

Parameter	Coefficient	σ
Intercept	-7.21	0.89
NK/Al melt	3.56	0.41
10000/T [K]	0.377	0.095
$^{\mathrm{W}}$F	1.25	0.31
R^2; PRESS	0.859	0.848

Model for LnD_{Li} (No T term; n = 43)

Parameter	Coefficient	σ
Intercept	-26.36	2.16
$^{\mathrm{VI}}$MFe^{2+}	4.89	0.76
$^{\mathrm{VI}}$MMg	3.05	0.58
$^{\mathrm{IV}}$TSi	6.08	0.65
	0.799	0.784

Model for LnD_{Li} (No F term; n = 43)

Parameter	Coefficient	σ
Intercept	-7.01	1.06
$^{\mathrm{VI}}$MFe^{3+}	-4.29	1.35
NK/Al melt	4.18	0.41
10000/T [K]	0.407	0.104
R^2; PRESS	0.840	0.828

Model for LnD_{Nb} (n = 47)

Parameter	Coefficient	σ
Intercept	12.5	2.4
$^{\mathrm{VI}}$MFe^{2+}	-5.17	1.20
$^{\mathrm{VI}}$MMg	-5.42	0.90
NBO/T melt	1.15	0.23
P [MPa]	-0.0011	0.0002
	0.716	0.689

Table 5 Coefficients for the prediction of element partitioning between biotite and silicate melt. Multiple linear regression reports generated during the calibration of these models are available in the Appendix.

This manuscript was revised following one round of review at Journal of Petrology [Preprint; v. R1; 16th Feb 2026] , PUBYEAR, Volu

List of supplementary files

Electronic appendix A (.kml): A waypoint file for field localities for the Canary Islands pyroclastic rock samples

Electronic appendix B (.xlsx) A spreadsheet containing (1) Compositions of starting materials for the IHPV experiments; (2) Experiment run conditions; (3) Electron microprobe (EPMA) major-element data for experiment and Canary Islands biotite; (4) EPMA major-element data for experiment and Canary Islands glass; (5) EPMA reference material measurements, including comparison to values retrieved from the GeoReM database (Jochum et al. 2005; compiled values from Govindaraju 1994); (6) Laser ablation ICP-MS measurements of Canary Islands biotite and glass; (7) Laser ablation measurements of experimental run products; (8) Laser ablation analyses of reference materials compiled across several measurement sessions, including comparison to compiled values retrieved from the GeoReM database (Jochum et al. 2005, 2011, 2016; Smith 1995; John Stix 2015 compilation) (9) Deconvolved analyses of biotite and glass via LA-ICP-MS; (10) Nernst partition coefficients (D values) for major- and trace-elements as determined from EPMA and LA-ICP-MS analyses; (11) and finally a spreadsheet for assigning biotite major-element ions to lattice sites following Li et al. (2020) modified after Zhang et al. (2022), for calculating silicate melt water speciation following Behrens (2020), and subsequently melt XF and XOH values, melt NBO/T following Mills (1993), and for determining modelled F-OH and Cl-OH exchange coefficients following Zhang et al. (2022), and F-OH exchange, ^{XII}A-site lattice strain parameters, D values for Na, K, Rb, Cs, Li and Nb using our new empirical partitioning models.

Electronic appendix C (.zip) A folder containing MATLAB scripts for reduction of laser-ablation trace-element measurements from both unmixed and mixed

Supplementary figures

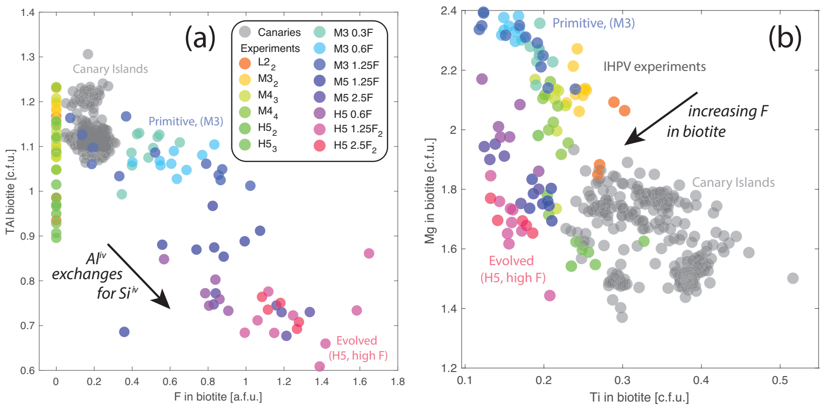

Figure S1 Major-element compositions of biotite from the Canary Islands pyroclastic rocks, compared with those produced in the internally heated pressure vessel experiments. (a) Tetrahedral Al vs. F content, (b) Mg vs. Ti content. Arrow shows compositional offset in biotite for the same experiment starting composition when fluorine is added. Ionic site assignments are calculated based on a total cation charge of 22 per formula unit.

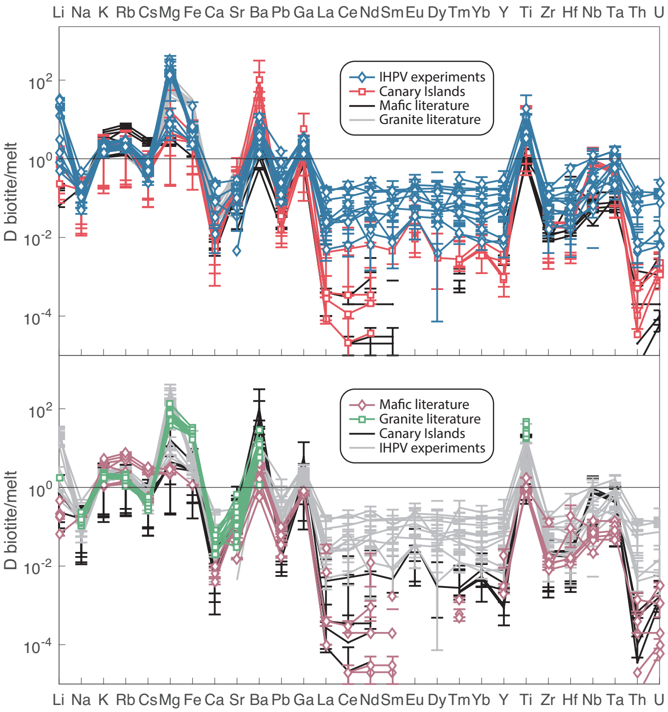

Figure S2 Biotite/melt element partition coefficients for experiments and Canary Islands pyroclastic rocks, including partition coefficients for the REE. Shown for comparison are published experimental partition coefficients for mafic compositions from Adam *et al.* (1993); LaTourrette *et al.* (1995); Schmidt *et al.* (1999); Green *et al.* (2000); Adam & Green (2006), and from granitic compositions from Icenhower & London (1995, 1997). Note how D_{La} is slightly higher than D_{Ce} in case of the Canary Island rocks and mafic experiments from Adam & Green (2006). Note that D_{REE} for the IHPV experiments from this study are unreliable, because the REE concentration in the biotite is at or below the detection limit of our LA-ICP-MS setup.

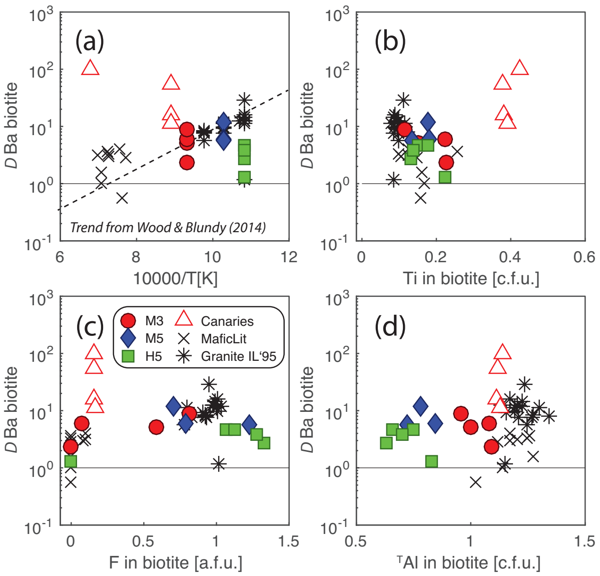

Figure S3 Barium partitioning vs. inverse temperature and compositional parameters for biotite. (a) follows Wood & Blundy (2014, literature data), where our experimental results for the M3 and M5 composition are consistent with trends defined by published D_{Ba} values (citation in prev. figs), with our Canaries samples returning consistently higher values for D_{Ba} and experiments on the H5 composition consistently lower. (b) shows that the elevated D_{Ba} values of the Canaries biotite are correlated with their high Ti contents. (c) shows a poor correlation between F in biotite and D_{Ba}, and (d) shows a weak positive correlation between tetrahedral Al and D_{Ba}. Literature data sources as listed in Fig. 6.

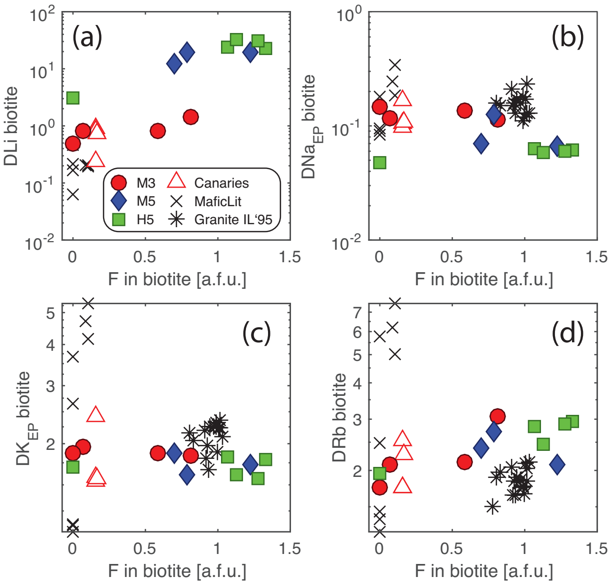

Figure S4 Partitioning of 1+ elements vs. fluorine content of the biotite, calculated on the basis of 22 charges per formula unit. Mafic literature data sources as listed in Fig. 6. IL'95 is Icenhower & London (1995).

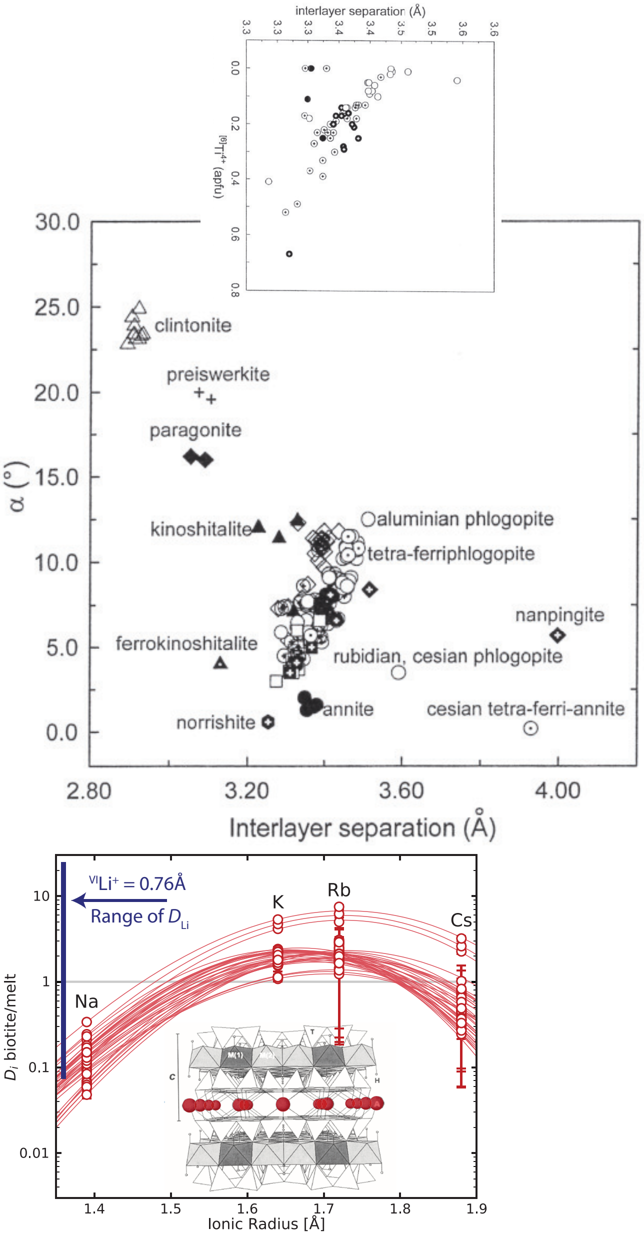

Figure S5 Onuma diagram for the partitioning of 1+ cations between the mica interlayer site and silicate melt. Interlayer separation diagrams from Brigatti & Guggenheim (2002) for comparison, where the radius scale is aligned to half of the interlayer separation value.

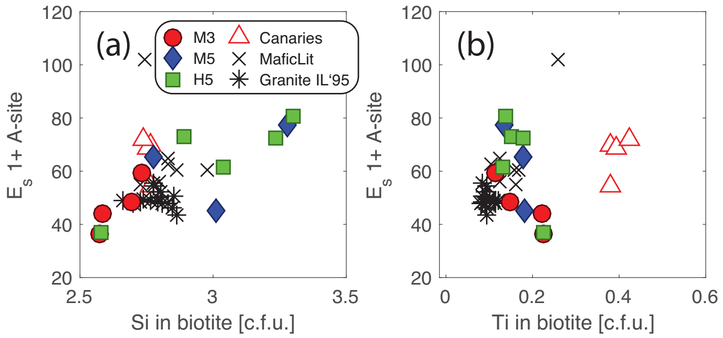

Figure S6 Young's modulus for 1+ ions in the A-site of biotite vs. compositional parameters.

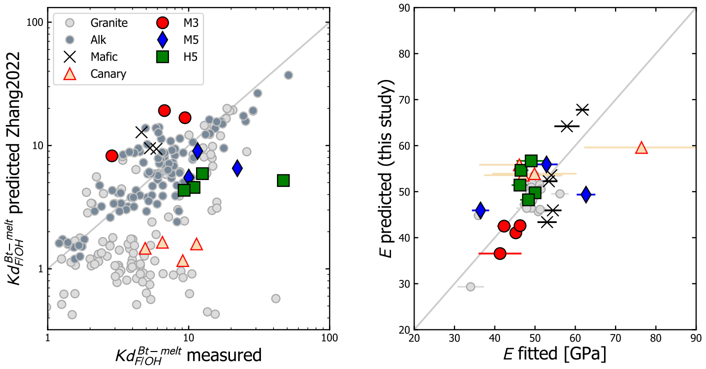

Figure S7 Measured vs. predicted diagrams for (left) Kd F-OH for the empirical model of Zhang *et al.* (2022), which broadly reproduces our experimental data set, but systematically underpredicts Kd values for the peraluminous granite experiments of Icenhower & London (1995) and our Canary Islands natural mineral-melt pairs. The right panel shows performance of our model for the E parameter of the lattice strain model for 1+ cations at the biotite XII-coordinated A-site.

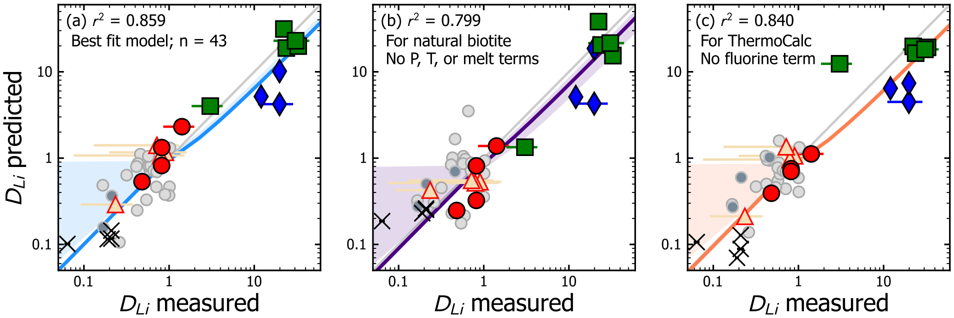

Figure S8 Measured vs. predicted diagrams for three contrasting empirical models for lithium partitioning between biotite and melt. The gray diagonal lines show 1:1 relationships between measured and predicted D_{Li} values. Coloured regression lines are robust fits to the partitioning data with uncertainty envelopes shown at the 1σ level.